JOURNAL OF GEOPHYSICAL RESEARCH, VOL. 105, NO. C10, PAGES 23,943–23,965, OCTOBER 15, 2000

Circulations and eddies over the South China Sea derived from TOPEX/Poseidon altimetry

Cheinway Hwang and Sung-An Chen

Department of Civil Engineering, National Chiao Tung University, Hsinchu, Taiwan

Abstract. TOPEX/Poseidon (T/P) altimeter data were used to derive time-varying circulation and eddies over the South China Sea (SCS) for 1993-1999. Large variabilities of sea surface heights and dense distribution of eddies were found to occur along a band across the SCS basin. A cross-over method is introduced to compute pointwise velocity components. The T/P-derived circulations and eddies are consistent with the drifter results from the World Ocean Circulation Experiment data center. (1) Because of monsoons, the SCS circulation is largely cyclonic in winter, is largely anticyclonic in summer, and is modulated interannually by El Niño – Southern Oscillation. (2) Both cold- and warm-core eddies were found in the waters east of Vietnam, west of Luzon, and west of the Luzon Strait, but their times of occurrence and the way they evolved vary interannually. (3) The reversal of the alongshore currents east of Vietnam was in complete accordance with wind stress. The locations and kinematic properties of eddies over SCS were estimated by the least squares method. The averaged vorticities of the cold- and warm-core eddies are 1.684×10^{-6} and -1.738×10^{-6} rad s^{-1}, respectively, and the shearing and stretching deformations are one thousandth of the vorticities. The angular velocity of eddy decreases with increasing radius. Coherence analysis suggests that the interannual and seasonal variations of circulation are largely due to wind stress, and the semi-annual variation is largely due to wind stress curl. The angular velocities of eddies over the central SCS basin are coherent with the magnitudes and signs of wind stress curl. The seasonal steric anomaly was also computed, and its spatial pattern and scale are quite different from those of circulation and eddy.

1. Introduction

In recent years the South China Sea (SCS) has attracted much attention from the oceanographic and geophysical communities. For example, scientists from east Asia, the United States, and Australia have joined the international project South China Sea Monsoon Experiment (SCSMEX) to study the water and energy cycles over SCS and its surrounding regions [*Lau*, 1997]. Figure 1 shows the major surface and bottom features of SCS. The SCS is a semiclosed sea with major water exchanges occurring at the Taiwan Strait to the north, at the Luzon Strait to the east, and at the Sunda Shelf to the south. Exchange of deep water can occur only at the Luzon Strait, where the water is sufficiently deep [*Nitani*, 1972]. According to the basic hydrodynamic equations [e.g., *Apel*, 1987, Chapter 3] the varying depths of 200 - 6000 m, the seamounts, the islands, the other shallow-water obstacles, and the monsoonal winds may well make the circulation and the eddy fields of SCS very complicated. The observation of the SCS circulation began with *Wyrtki* [1961]. The most recent large-scale drifter observation of the SCS circulation is attributed to *Hu* [1998], who reported seasonal variation of the SCS circulation. The numerical models of both *Shaw and Chao* [1994] and *Wu et al.* [1998] suggest that the SCS circulation is mostly wind-driven. *Shaw and Chao*'s [1994] model also shows, among other features, a strong coastal current east of Vietnam, which is southward in summer and northward in winter. The model of *Wu et al.* [1998] indicates that interannual variation of the SCS velocity field are noticeable during El Niño. *Metzger and Hurlburt* [1996] modeled the coupled dynamics between SCS and the surrounding seas, concluding that the circulation interior to SCS is significantly affected by the wind curl field, especially the cyclonic gyre and the coastal currents off southern China and Vietnam. *Metzger and Hurlburt* [1996] also show that the primary mechanism of the seasonal inflow and outflow of water at the Luzon Strait is the wind stress pileup from the monsoon. Furthermore, eddy observations over SCS date back to the work of *Dale* [1956], who reported a cold-core eddy off east Vietnam in summer. The most recent in situ observation of the SCS eddies is due to *Chu et al.* [1998a], who discovered dual anticyclonic eddies in the central SCS basin and cyclonic eddies associated with the former. The mechanism of the formation of these eddies was later explained by *Chu et al.* [1998b]. The first use of mixed remote sensing data for eddy detection over SCS was made by *Soong et al.* [1995], who discovered a cold-core eddy west of Luzon using TOPEX/Poseidon (T/P) altimetry, advanced very high resolution radiometer (AVHRR) temperature images, and drifter data. Later, *Kuo and Ho* [1998] discovered a cold-core eddy east of Vietnam using AVHRR, and they attributed this cold-core eddy to coastal upwelling. [e.g., *Grüdlingh*, 1995; *Meyers and Basu*, 1999; *Siegel et al.*, 1999]. Recently satellite altimetry has been increasingly used as a remote sensing tool to identify eddies.

Paper number 2000JC900092.
0148-0227/00/2000JC900092$09.00

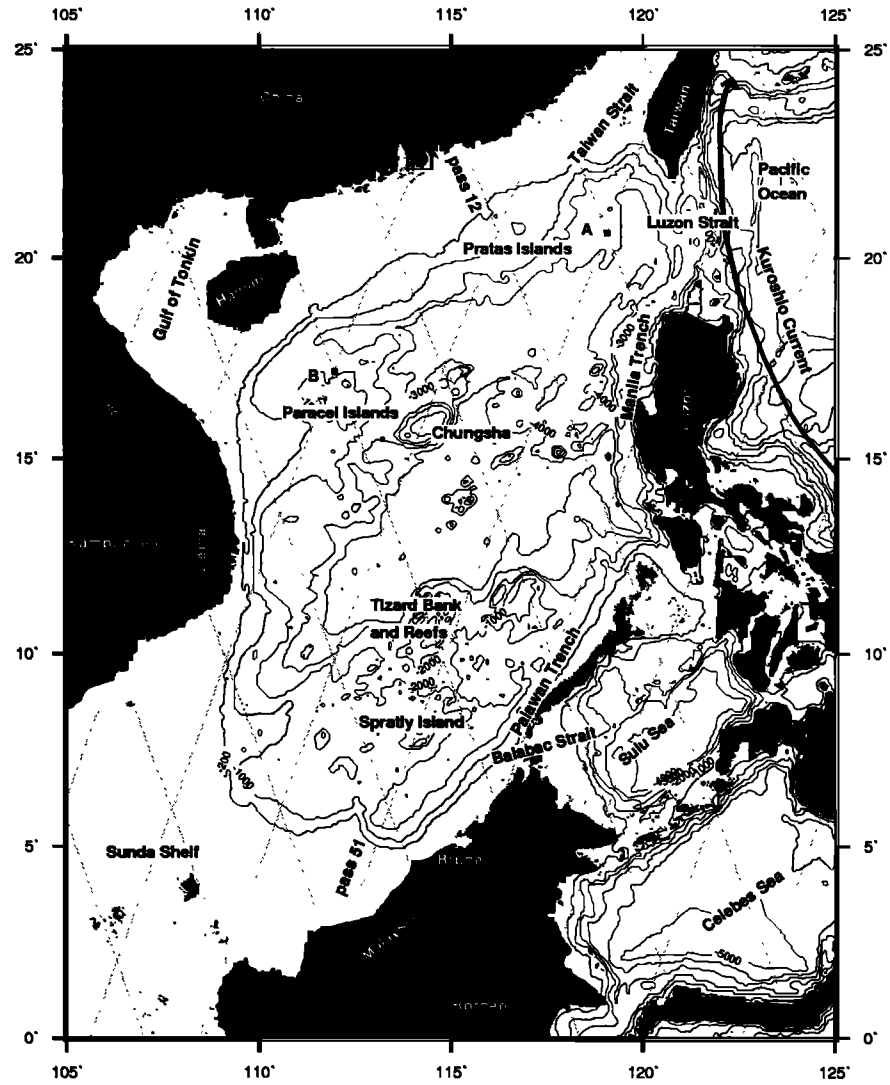

Figure 1. Major surface and bottom features and selected contours of depth over the SCS. The letters A and B indicate two crossovers of T/P ground tracks (dots). A number near a T/P track is the pass number.

Despite the huge effort in the past the existing observations of the SCS circulation and eddy field remain quite scattered compared to the size of SCS. This scattering makes it difficult to see the spatial and temporal evolution of circulation and eddy field over SCS, which are now largely based on numerical models. With the advent of satellite altimetry this sampling problem can be mitigated because altimetry can provide data of continuous coverage in space and time. In particular, altimeter data are very useful for the study of time-varying circulation because there is no need of the geoid in this case [*Wunsch and Stammer*, 1998]. Interestingly, while the sea level of SCS has been extensively studied with satellite altimetry [e.g., *Shaw et al.*, 1999; Hwang and Chen, 2000], the circulation and eddy field of the SCS have not received the same attention with altimetry; that satellite altimetry can be used to derive meaningful circulation and eddies in a marginal sea like SCS is not known with certainty. Accordingly, this study will focus on the derivations of the SCS circulation and eddy field using the best altimeter data to date: the T/P data, with an aim to discover phenomena not found in the existing observations and numerical models and to verify existing theories by the altimetry result. In the following we first describe the T/P data processing, then introduce methods to compute time-varying circulation and to locate eddies. T/P-derived circulation and eddies are then compared with drifter velocities. Next, we show the T/P-derived climatological circulation of SCS and the kinematic properties of eddies and describe the characteristics of their seasonal and interannual variations associated with El Niño/Southern Oscillation (ENSO). We will use NINO3 Sea Surface Temperatures (SSTs) as the index of ENSO. As defined by *Kiladis and Diaz* [1989], during the time span of this study, i.e., from 1993 to 1999, there are three El Niños, occuring in 1992-1993, 1994-1995, and 1997-1998, and one La Niña, occuring in 1995-1996. Finally, we discuss the relationships between wind and some interesting phenomena and point out the possible causative mechanisms.

2. Data Processing and Analysis Methods

2.1. T/P Altimeter Data Processing

T/P is an altimetry mission dedicated to measuring the ocean topography and circulation [*Fu et al.*, 1994]. With its unprece-

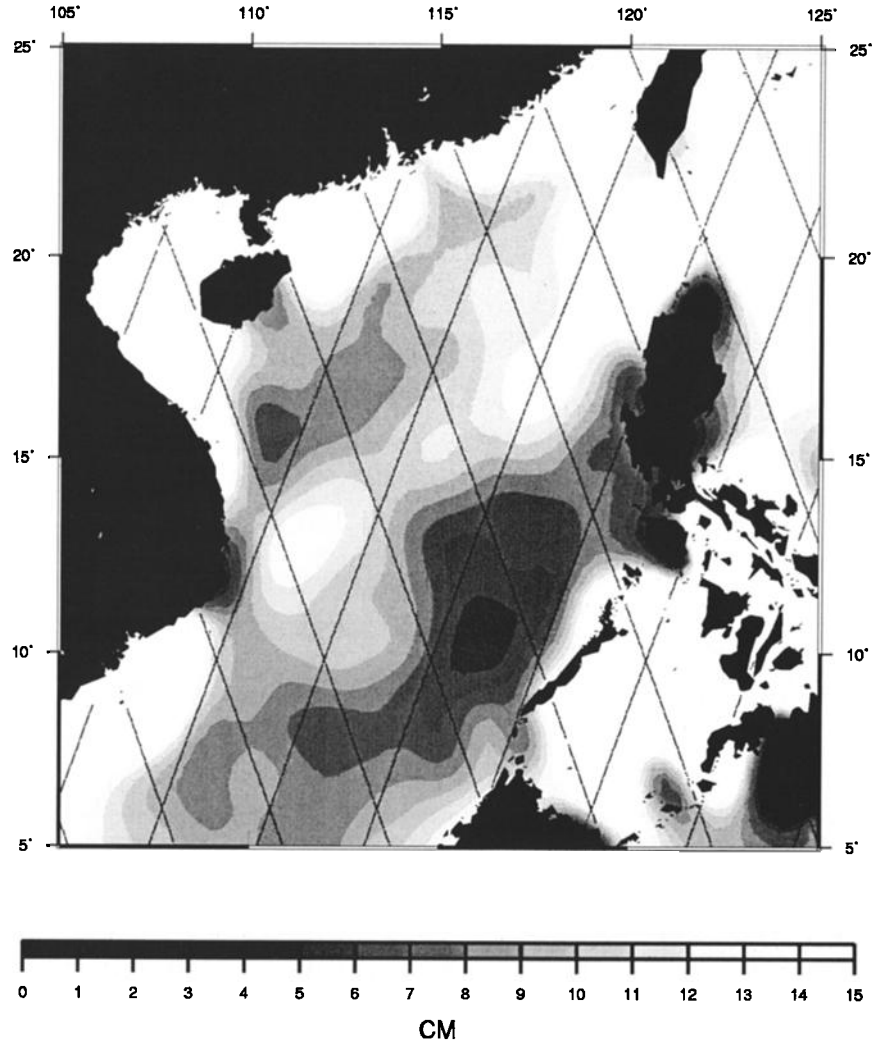

Figure 2. Sea surface height variabilities derived from 5.6 years of T/P altimeter data.

dented accuracy and nominal 10 day (actually 9.9156 days) repeat period, T/P is an important tool for deriving spatial and temporal variabilities of the ocean. In this study we used the T/P version C Geophysical Data Records (GDRs) from Archiving, Validation and Interpretation of Satellite Oceangraphic data (AVISO) [1996] to generate geophysically corrected sea surface heights (SSHs) from T/P cycle 10 (December 26, 1992) to cycle 219 (August 29, 1998). In particular, we have removed the ocean tide based on the CSR3.0 tide model [*Eanes and Bettadpur*, 1995]. The first nine cycles were not used because of the mispointing problem [*Fu et al.*, 1994]. Other details of the T/P data processing were described by Hwang and Chen [2000], who used the same T/P data as those used in this study to perform Fourier and wavelet analyses of the SCS sea level. In fact, we have created a T/P database that requires only two simple commands to extract SSHs or sea level anomalies for any given area and cycles using the efficient algorithm described by *Hwang et al.* [1998]. We also averaged SSHs from the 210 T/P cycles (total 5.6 years) to yield along-track mean SSHs for subsequent analyses. Figure 2 shows the SSH variability over SCS derived from this averaging process. The anomalous variability over the continental shelf is mainly due to the aliasing of ocean tides [Hwang and Chen, 2000] and should be discarded. The variability is largest around the Luzon Strait, where water exchange between SCS and the Kuroshio Current occurs. In the areas east of Vietnam and west of Luzon the variability is also relatively large. In general, large variability occures along a band across the SCS basin in the northeast-southwest direction. Normally, large SSH variability is associated with strong circulation and eddy activity, as will be demonstrated in section 3.

An important issue is whether the tidal aliasing contained in T/P data will affect the result in this paper. The model error of CSR3.0 over the SCS, especially the tidal aliasing problem, has been analyzed by Hwang and Chen [2000], who show that CSR.3.0 has the largest error over the continental shelf and the least error in the central SCS basin. Although tidal model error is a complex function in space and time, it can be reduced by spatial filtering and temporal averaging. For example, the three longest wavelengths of the aliasing *M2* in T/P are 9°, 4.14° and 2.16°. Employing the median filter with a 300 km wavelength on the TP/SSHs, the 2.16° alias can be remove and the 4.14° alias can be reduced substantially. The 9° alias has a spatial scale that is too large to affect the results presented in this paper. The median filter, which will be used by outliers [*Naess and Bruland*, 1989]; outliers are very common in the surface data collected in the SCS because

the SCS is frequently visited by violent typhoons. The choice of 300 km is based on the cross-track spacing of T/P (2.83°) and the requirement that the detail of SSH be retained while removing false signals. Also, as shown by *Hwang* [1997, Table 5], at a given location a 10 cm *M2* model error in T/Pcan be reduced to 2.26 and 0.41cm by averaging T/P data over 3months and 1 year, respectively. Nevertheless, because of the large tidal model errors over the continental shelf of the SCS including the Sunda Shelf, we ignore any result there in this paper Another issue is whether the T/P data noise will produce false signals To investigate this, we produced a smooth dynamic topography field by subtracting the Earth Gravitational Model 1996 (EGM96) geoid [*Lemoine et al*, 1998] from the 5.6 year averaged SSHs (see section 2.2.1 for the definition of dynamic topography). We then added random noises to the dynamic topography based on a 4.7 cm standard error [*Fu et al.*, 1994]. Finally, We used the median filter to smooth the original and the noise-disturbed dynamic topography fields. Contour plots of two smoothed dynamic topography fields show that they are almost identical (the plots are not shown because of limited space), and this similarity suggests that the T/P noises can be effectively eliminated by the median filter. Other evidence in the following development will also show that the T/P tidal aliasing and noise will not affect the result in this paper.

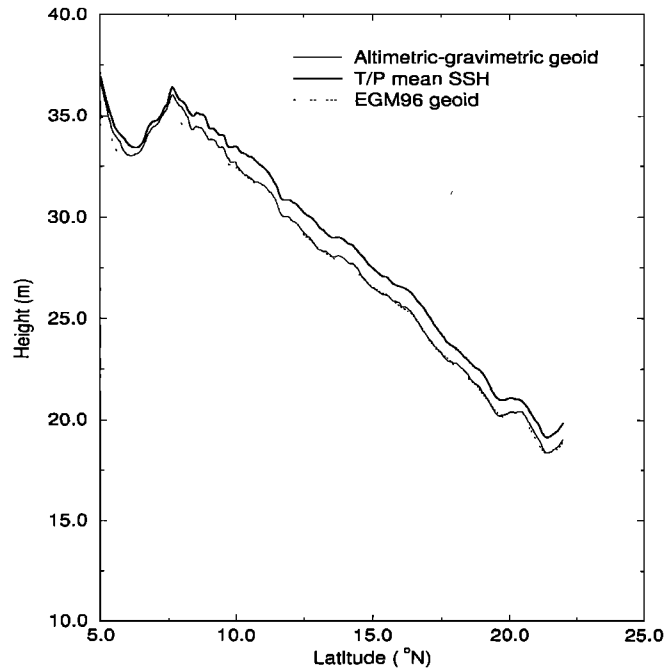

Figure 3. Comparison of altimetric-gravimetric geoid, EGM96 geoid, and T/P mean SSH along T/P pass 51.

2.2. Analysis Methods

2.2.1. Computing geostrophic velocity on a grid. In this case the dynamic heights from altimetry are first interpolated on a grid, then the horizontal components of geostrophic velocity are computed by [*Apel*, 1987]

$$u = -\frac{g}{f}\frac{\partial \zeta}{R\partial \phi} = -\frac{g}{f}\frac{\partial \zeta}{\partial y} = -\frac{g}{f}\xi \tag{1}$$

$$v = \frac{g}{f}\frac{\partial \zeta}{R\cos\phi \partial \lambda} = \frac{g}{f}\frac{\partial \zeta}{\partial x} = \frac{g}{f}\eta\ , \tag{2}$$

where ζ is the dynamic height; u and v are the east and north velocity components, respectively; g is gravity, $f = 2\Omega\sin\phi$, with Ω being the earth's rotational rate (7.292115×10^{-5} rad s^{-1}), R is the mean radius of the Earth, ϕ and λ are the latitude and longitude; and x and y are the local rectangular coordinates, with positive x to the east and positive y to the north. The dynamic height is the difference between SSH, h, and the geoidal height, N:

$$\zeta = h - N \tag{3}$$

The problem with this approach is that an accurate geoid over the oceans is difficult to compute. Currently, there exist geoid models over SCS, for example, the model of *Hwang* [1996], but the accuracies of these models may not be sufficient to resolve circulation and eddy at the mesoscale level. However, if we are only interested in the time-varying circulation, we need only the relative dynamic height [*Wunsch and Stammer*, 1998]

$$\Delta\zeta = \zeta - \zeta_0 = h - h_0 = \Delta h\ , \tag{4}$$

where ζ_0 is the time-independent dynamic height and h and h_0 are the instantaneous (after removing the tidal effect) and mean SSH from altimetry. Replacing ζ by $\Delta\zeta$ (in reality, Δh, the sea level anomaly) in (1) and (2), one obtains the relative geostrophic velocity. It is noted that the T/P mean SSHs averaged over 210 cycles are rather close to some existing geoids over SCS and have accuracies better than 1 cm. As an example, Figure 3 compares the T/P mean SSH, the altimetric-gravimetric geoid of *Hwang* [1996] and the geoid from the EGM96 gravity model to degree 360 [*Lemoine et al.*, 1998] along T/P pass 51 (see Figure 1). Apart from a constant bias, the first two agree quite well. Note that since the goal of this study is to derive the time-varying circulation and eddies from T/P, relative dynamic height will be always used, and the computed velocities in this paper are always the relative (time-varying) geostrophic velocities. The word "relative" will be omitted in the following development. Furthermore, on the basis of EGM96 dynamic topography model [*Lemoine et al*, 1998] the mean circulation of SCS is very small compared to the climatological circulation. Thus, in most areas of SCS the relative geostrophic flow derived with $\Delta\zeta$ will closely resemble the absolute geostrophic flow derived with ζ, except near the Luzon Strait, where water exchange between SCS and the Pacific occurs and the Kuroshio Current will contribute a significant mean flow.

In the actual computations of time-varying geostrophic circulation, for each T/P cycle we first found the median dynamic heights in $1°\times1°$ boxes, which were then used to construct a $1°\times1°$ grid using the minimum curvature interpolating scheme with a tension factor of 1 (a tension factor of 1 will make the grid as smooth as possible) [*Smith and Wessel*, 1990]. Contour plots of such grids show many unrealistic signatures; thus at the final stage we employed the median filter with a 300 km wavelength to smooth the $1°\times1°$ grid. At each of the grid points we evaluated the coefficients of a quadratic polynomial that best fits the dynamic heights around this grid point. Then the first derivatives along the

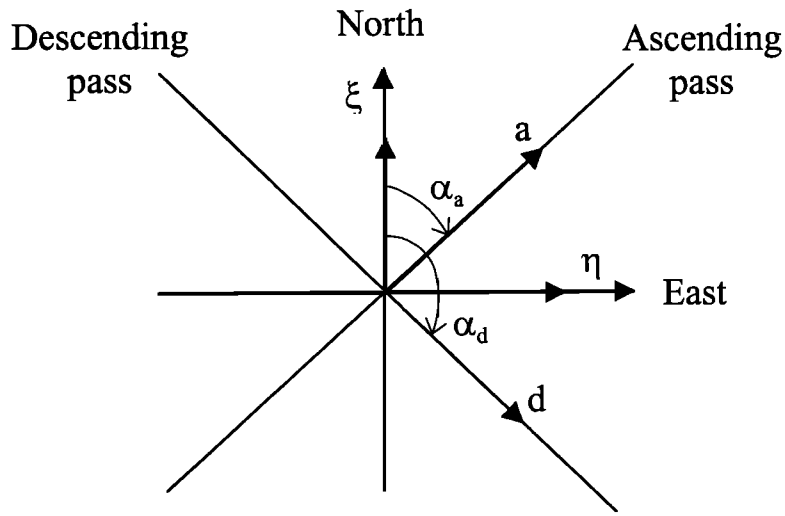

Figure 4. Ascending (a), descending (d), north (x), and east (h) components of gradient of the dynamic height at a crossover of two ground tracks.

east and north directions were obtained from the quadratic polynomial and used to derive the velocity components by (1) and (2). For each cycle the times associated with all gridded velocities are the same and are the central time of this cycle.

2.2.2. Computing pointwise velocity at a crossover. In this case we are interested in the velocity components at a single point. It turns out that such a pointwise computation is possible only at the crossover of an ascending track and a descending track Referring to Figure 4, the gradients of the dynamic heights along the ascending and descending tracks, a and d, are [*Heiskanen and Moritz*, 1985, p. 187)

$$a = \xi \cos\alpha_a + \eta \sin\alpha_a \tag{5}$$

$$d = \xi \cos\alpha_d + \eta \sin\alpha_d \tag{6}$$

where η and ξ are the east and north components of gradient (see (1) and (2)), respectively, and α_a and α_d are the azimuths of the ascending track and the descending track at the crossover, respectively. Inverting (5) and (6) leads to

$$\eta = \frac{a\cos\alpha_d - d\cos\alpha_a}{\sin(\alpha_a - \alpha_d)} \tag{7}$$

$$\xi = \frac{-a\sin\alpha_d + d\sin\alpha_a}{\sin(\alpha_a - \alpha_d)}\,, \tag{8}$$

which can be used to derive velocity components by (1) and (2). The along-track gradients of the dynamic height can be computed by numerical differentiation, as was used in deriving the along-track deflections of the vertical [*Hwang et al*, 1998]. Gradients derived in this way will contain negligibly long wavelength effects because of orbit error and low-frequency tidal model error [*Hwang*, 1997]. Using this method, T/P is like a current meter that measures the geostrophic velocity at a crossover every 10 days. This method can be used to identify the type of an eddy and compute its velocity if a T/P (or any T/P class altimeter) crossover is located inside the eddy. For example, the crossover of T/P passes 12 and 51 is located to the west of Luzon (see Figure 1), so here one can compute the eddy velocity of the cold-core eddy discovered by *Soong et al* [1995], who simply computed the velocity components perpendicular to passes 12 and 51 at selected spots.

However, this crossover method requires very accurate dynamic height. To see this, we can derive the 1σ errors of the east and north velocity components from (1), (2), (7), and (8) using error propagation:

$$\sigma_u = \frac{g}{f}\frac{\sqrt{\sin^2\alpha_a + \sin^2\alpha_d}}{|\sin(\alpha_a - \alpha_d)|}\sigma_g \tag{9}$$

$$\sigma_v = \frac{g}{f}\frac{\sqrt{\cos^2\alpha_a + \cos^2\alpha_d}}{|\sin(\alpha_a - \alpha_d)|}\sigma_g\,, \tag{10}$$

where σ_g is the 1σ error of the gradient, which is the same for the ascending and the descending gradients. In deriving (9) and (10) we assume that the errors of velocities are solely from the gradient components (the errors of azimuths will also make contribution but are neglected). A rough estimate of σ_g is [*Hwang et al.*, 1998]

$$\sigma_g = \frac{\sqrt{2}}{s}\sigma_h\,, \tag{11}$$

where σ_h is the 1σ error of the dynamic height and s is the along-track sampling interval. Because of T/P's inclination angle of 66°, which yields a relatively inaccurate east component of gradient, the v component has a much larger error than that of the u component. Assuming a 1 cm error for the mean SSH (or the geoid, in the case of absolute velocity), a 4.7 cm error for one single T/P-measured SSH [*Fu et al.*, 1994, Table 2], and s = 6.2 km, we have $\sigma_g \approx 10.9\times10^{-6}$ rad. With this σ_g value we find that $\sigma_u \approx 160$ cm s^{-1} and $\sigma_v \approx 400$ cm s^{-1} at crossover A and $\sigma_u \approx 189$ cm s^{-1} and $\sigma_v \approx 410$ cm s^{-1} at crossover B (see Figure 1). Clearly, by this method, T/P can detect only very large geostrophic currents at the 6.2 km wavelength. However, the long wavelength

component of geostrophic current can be determined with an improved accuracy using filtered along-track dynamic heights.

2.2.3. Identifying eddy and computing its kinematic properties. In this study the identifications of eddies implied in the T/P data will be based on the contour plots of the dynamic height and plots of circulation. This approach has been used by, for example, *Grundlingh* [1995], *Siegel et al.* [1999], and *Crawford and Whitney* [1999]. An automatic edge detector may be used to detect an eddy [e.g., *Meyers and Basu*, 1999], but the complex land-ocean geometry of SCS and the relatively poor T/P data quality over the SCS will require a further, very subjective judgment before one can decide whether a detected eddy is reasonable and acceptable. An eddy will create a circle-like shape in the contour plot of dynamic height, and the derived circulation will show a signature of eddy (see also the plots of circulation below). Note that a propagating wave or an aliasing tide will also create sea surface elevations, but one whose contours are mostly noncircular and deformed [see also *Schlax and Chelton*, 1994]. Considering the accuracy of T/P dynamic height, in this paper the edge of an eddy is defined to be the 5 cm contour of dynamic height counting from the center of the eddy [see also *Grundlingh*, 1995]. The center of an eddy is estimated using the contour plots and will be later revised by the least squares method discussed below. The radius of the eddy is defined to be the averaged distance from the center to the edge on a Mercator projection. The distortion of distance in the Mercator projection over the SCS is small because SCS is near the equator. The distortion is also very small compared to the uncertainty in position. To compute the kinematic property of an eddy, we adopt the models used by *Okubo* [1970], *Kirwan et al* [1984] and *Sanderson* [1995]. First, in the local rectangular coordinate system, the velocity gradients of an eddy are

$$g_{11} = \frac{\partial u}{\partial x}, g_{12} = \frac{\partial u}{\partial y}, g_{21} = \frac{\partial v}{\partial x}, g_{22} = \frac{\partial v}{\partial y}, \tag{12}$$

where the definitions of u, v, x, and y are the same as those in (1) and (2) and g_{ij}, etc., are velocity gradients, which are assumed to be constants. The four kinematic properties to be computed are

$$\text{vorticity} = 2 \times \text{angular velocity} = g_{21} - g_{12},$$
$$\text{divergence} = g_{11} + g_{22},$$
$$\text{stretching deformation} = g_{11} - g_{22},$$
$$\text{shearing deformation} = g_{21} + g_{12}.$$

In the Northern Hemisphere the vorticity is positive for a cyclonic eddy and is negative for an anticyclonic eddy. For a perfectly circular eddy with a uniform angular velocity, only the vorticity is nonzero. The vorticity can be interpreted as the fluid circulation per unit area. Given the T/P-derived velocities, the velocity gradients and the coordinates of the eddy center, x_0, y_0, can be estimated using the following model:

$$u(t) + e_u = g_{11}[x(t) - x_0] + g_{12}[y(t) - y_0] \tag{13}$$

$$v(t) + e_v = g_{21}[x(t) - x_0] + g_{22}[y(t) - y_0], \tag{14}$$

where e_u and e_v are the residuals of the observed u and v velocity components and t is the time of the observation. In this model we have assumed that the flow velocity of the eddy at the center is zero. This assumption is reasonable over a semiclosed sea like the SCS but may not be valid over areas with energetic flows like the Kuroshio Current and the Gulf Stream. The nonlinear observation equations in (13) and (14) can be linearized using Taylor's expansion to the first-order term, and the parameters can be estimated by the least squares method. Appendix A describes the detail of our least squares method. An eddy is considered existent and its kinematic properties considered acceptable only if (1) the normal matrix $\mathbf{A}^T\mathbf{A}$ in (A6) is positive definite, (2) iterations in the least squares estimation converge, and (3) the sign of the computed vorticity matches the type of the eddy (positive for cold-core eddy and negative for warm-core eddy).

3. Results

3.1. Verification

3.1.1. Comparison of velocities. We first verify the T/P-derived velocities and eddies before doing any analysis of such results. To this end we obtained velocities measured with drifters over the SCS. The drifter data were mostly collected by *Hu* [1998] and were edited by *Hansen and Poulain* [1996], and are available at the World Ocean Circulation Experiment (WOCE) data center. *Hu* [1998] also presented a preliminary analysis of the SCS circulation based on these drifters. Figure 5 shows the tracks of selected drifters over the SCS, with some in the waters east of Taiwan and the Philippines. These drifter data were collected during 1993-1997 From Figure 5, in winter most of the drifters released at the Luzon Strait traveled in the anticlockwise direction and along the western boundary of the SCS. Drifter 20602 entered the SCS, circled off the shore of the southwestern Taiwan, and finally, moved to the Pacific Ocean. Drifter 459 first circled around an anticyclonic gyre east of Taiwan and then entered the SCS via the Luzon Strait. Thus the tracks of drifter 20602 and 459 were indicative of water exchange between the SCS and the Kuroshio Current as described by *Shaw* [1991]. The track of drifter 19801 indicates that an anticyclonic eddy existed east of Vietnam. The track of drifter 20616 shows a cyclonic eddy west of Luzon in January 1994, which was also detected by *Soong et al* [1995] using this same drifter and other data.

For comparison, the velocity components from T/P at the measuring times and locations of drifters were computed from the 10 day 1°×1° dynamic height grids using three-dimensional polynomial interpolations in latitude, longitude, and time. (Because of the low spatial and temporal resolutions of the T/P velocities as compared to the drifter velocities, any reasonable interpolation methods will yield the same result in this case [see also *Gerald and Wheatley*, 1994, p. 274] for the expected error of polynomial interpolation. Figure 6 compares the T/P-derived and the measured velocity components for six selected drifters of relatively long lifetimes. Excluding anomalous velocities and tidal currents, the temporal and spatial ranges of drifter velocities are roughly from 0 to 80 cms^{-1}. It must be pointed out that, velocities measured with a drifter contain geostrophic, inertial, tidal, and other currents [*Apel*, 1987], while the T/P-derived velocities contain only the geostrophic component In addition, the T/P-derived

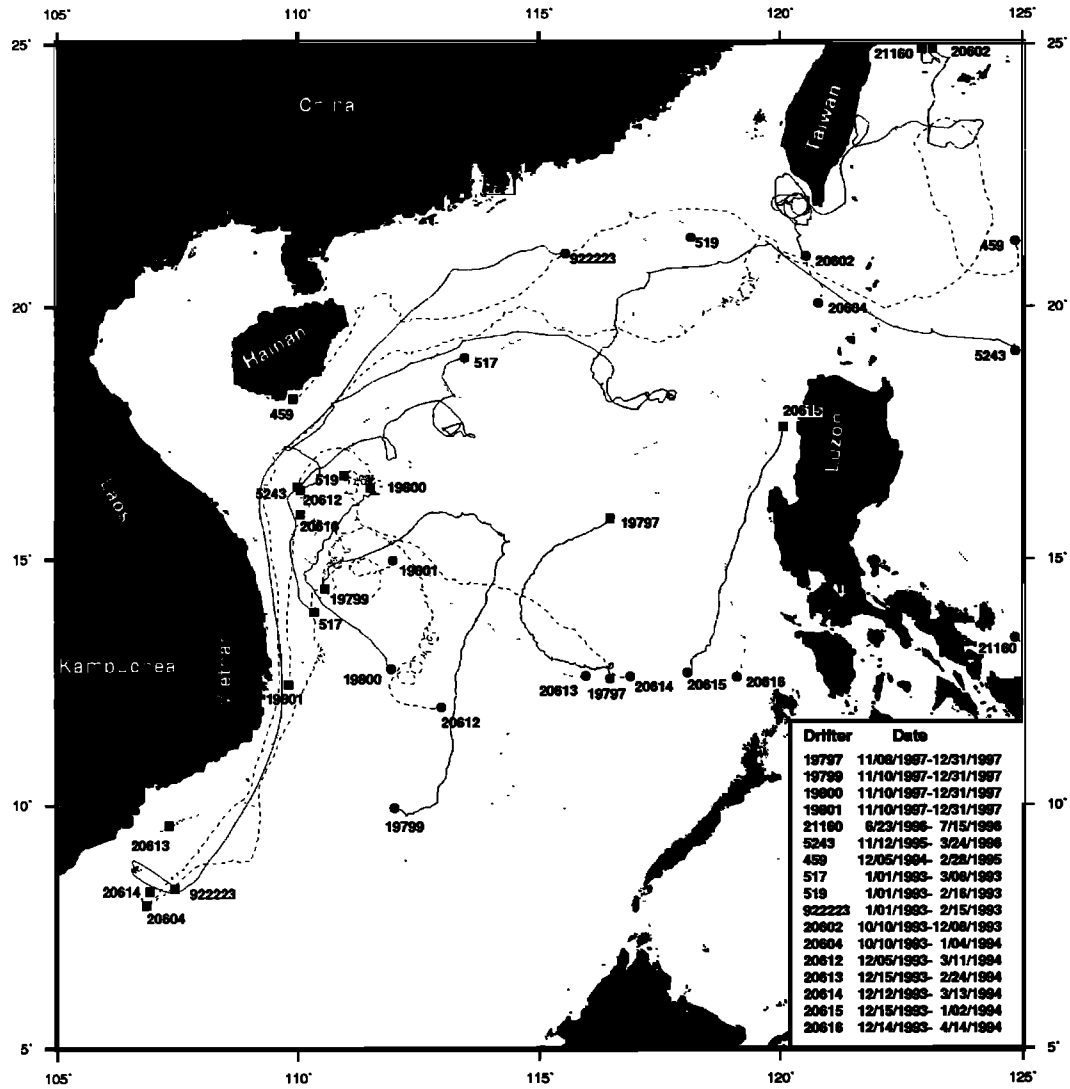

Figure 5. Tracks of selected drifters from the WOCE data center. Circles and squares indicates the starting and ending locations of tracks. Inserted is a box showing the starting and ending times of drifters in the studied area.

velocities are sampled at a 10 day interval, while the drifter velocities are sampled at a 6 hour interval. The T/P-derived velocities also have much lower spatial resolutions than those of drifter velocities because of the large cross-track spacing of T/P and the use of the median filter. From Figure 6 the T/P-derived velocities agree well with the drifter velocities at low frequencies. The overall directions of flow from T/P are consistent with those from the drifters. The T/P-derived velocities have the poorest fit, with the drifter velocities near the continental shelf of the SCS, where T/P data are less accurate and data gaps degrade the accuracy of interpolation. The drifter velocities are highly oscillatory. As an example, Figure 7 shows the periodograms of the measured east and north components of velocity from drifter 19799, which traveled in the waters east of Vietnam. Figure 7 indicates that most of the high-frequency oscillations of drifter 19799 are at frequencies of 0.5 and 1 cycle day^{-1} because of tidal currents.

3.1.2. Comparison of eddy kinematic properties. To see the comparison of eddy kinematic properties, we computed the kinematic properties of the cold-core eddy west of Luzon from the data of drifter 20616 and from the dynamic heights of T/P cycle 48 (mean time: January 7, 1994). The comparison is given in Table 1. In estimating the kinematic properties of this eddy we forced the center of the eddy determined from the drifter to be the center of the T/P-estimated eddy because the sparse drifter data have yielded large errors in the estimated eddy center. On the basis of Table 1 the vorticities and shearing deformations derived from the two data sets agree quite well, but the stretching deformations and divergences have large deviations, which are probably due to the different geographic distributions of drifter data and T/P data over this eddy.

3.2. Seasonal and Interannual Variations of the SCS Circulation

In the past, seasonal and interannual variations of the SCS circulation have been largely based on numerical models, for example, the models of *Shaw and Chao* [1994] and *Wu et al.* [1998]. With satellite altimetry, for the first time we will be able to observe these variations. We have computed maps of the monthly circulation from August 1993 to July 1998 using the gridded dy-

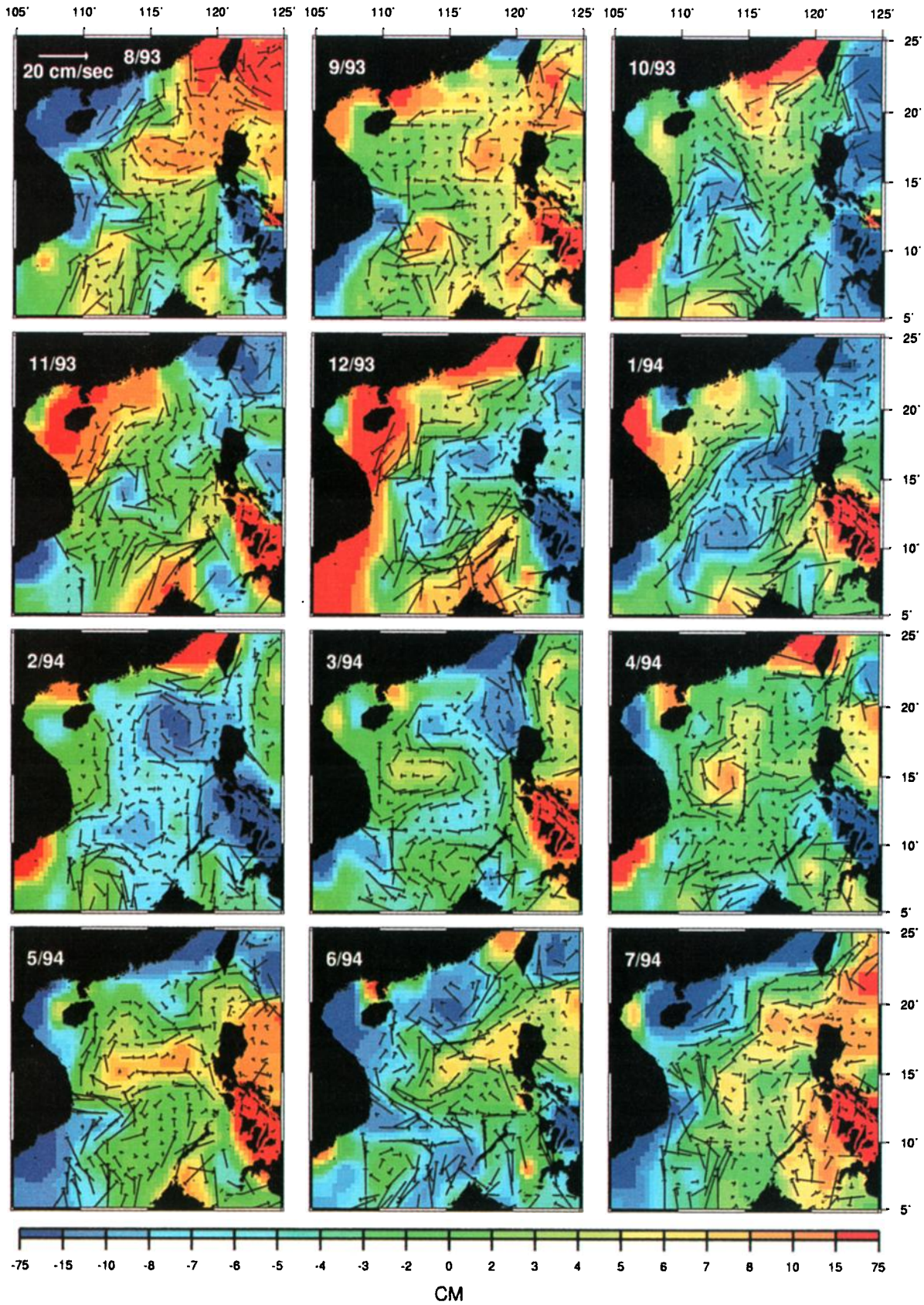

Plate 1. The relative dynamic heights and the monthly circulations of the South China Sea from August 1993 to July 1994 derived from T/P altimetry. The months and years are indicated on the upper left-hand corners. Monthly circulations in other years can be seen at http://space.cv.nctu.edu.tw.

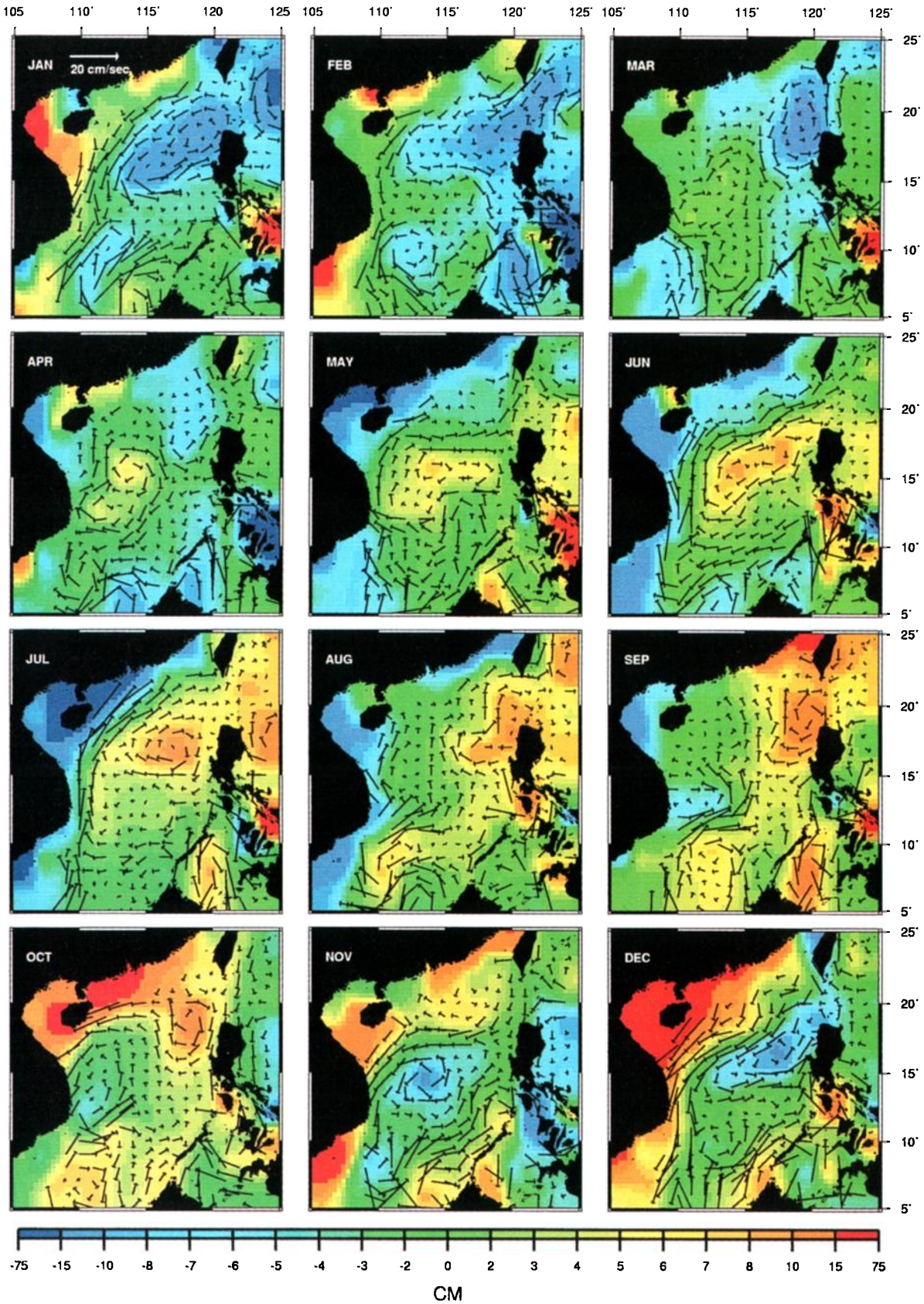

Plate 2. Same as Plate 1 but for 5 year averaged monthly circulations over 1993-1999.

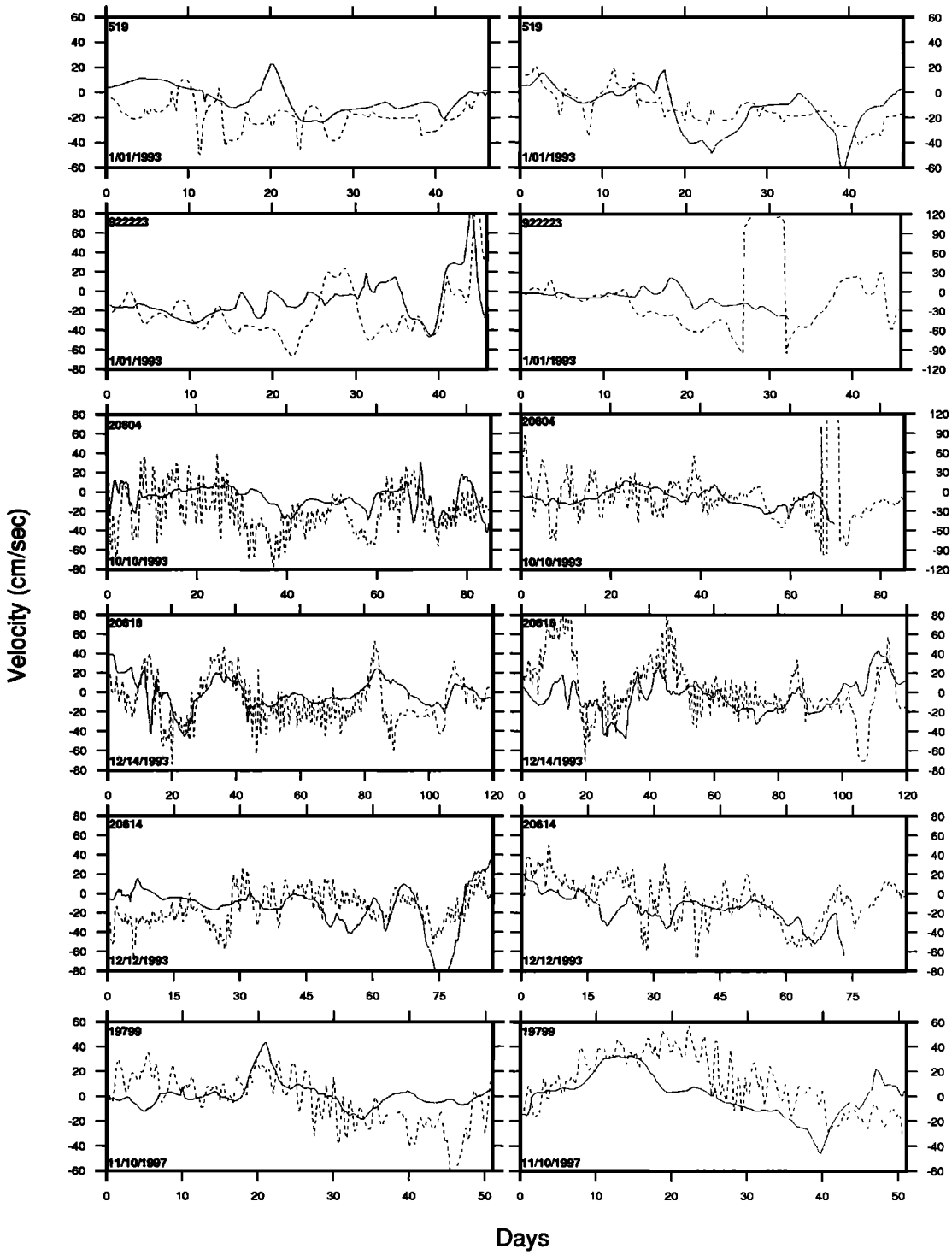

Figure 6. Comparison of T/P-derived (solid lines) and drifter-measured (dotted lines) velocities for six selected drifters: (left) The east component and (right) the north component. For each drifter the numbers are indicated in the upper left-hand corners, and the date of the first data points are indicated in the lower left-hand corners. Days are the elapsed days since the first data point.

namic topography values. As an example, Plate 1 shows the monthly circulations from August 1993 to July 1994. We also computed the 5 year averaged monthly circulation using

$$\bar{u}^{m}_{i,j} = \frac{\sum_{k=1}^{5} u^{m}_{i,j}(t_k)}{5}, i = 1,\cdots,I, j = 1,\cdots,J, m = 1,\cdots,12 \quad (15)$$

$$\bar{v}^{m}_{i,j} = \frac{\sum_{k=1}^{5} v^{m}_{i,j}(t_k)}{5}, i = 1,\cdots,I, j = 1,\cdots,J, m = 1,\cdots,12 , \quad (16)$$

where i, j, k, and m are indices of longitude, latitude, year, and month, respectively, and I and J are the numbers of points in the longitudinal and latitudinal directions, respectively. The 5 year

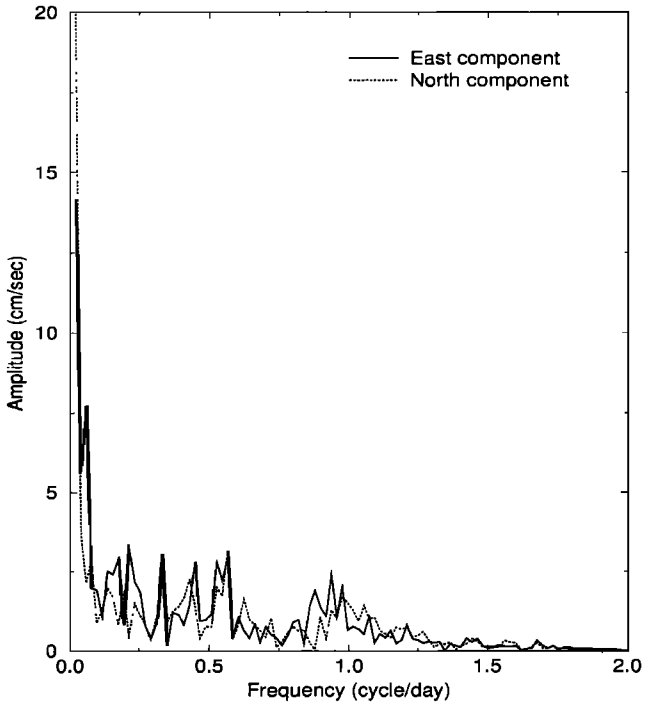

Figure 7. Periodograms of the velocities measured with drifter 19799.

averages are given in Plate 2. Most of the large-scaled features in Plate 1 and 2 agree well with those described by *Shaw and Chao* [1994] and *Wu et al* [1998], but T/P provides much better spatial and temporal resolutions. The directions of currents and the locations of eddies are consistent with those indicated by the tracks of the drifters in Figure 5. For example, the cyclonic eddy west of Luzon detected by drifter 20616 in January 1994 is clearly seen in Plate 1. Below is a summary of the seasonal and the interannual patterns of the SCS circulation based on Plate 1 and 2 and plots of monthly circulations in other years (not shown here but available at http://space.cv.nctu.edu.tw).

3.2.1. Winter (December to February). In the northern SCS and in the waters west of Luzon and east of Vietnam, there exist cold-core, cyclonic eddies. In general, the overall direction of flow in winter is cyclonic. In particular, strong southward alongshore currents are present at the western boundary of the SCS, with the strongest ones occurring off Vietnam. In the early springs of 1995, 1997, and 1998 the eddies east of Vietnam were anticyclonic (warm-core), rather than cyclonic as in the early springs of 1994 and 1996. This early warming of the SCS water may be associated with the 1994-1995 and the 1997-1998 El Niños At the Luzon Strait the flows are mostly westward, suggesting that the water of the Pacific Ocean enters the SCS in winter.

3.2.2. Spring (March to May). The SCS circulation is weakest in this season. In the northern SCS, there still exist cold-core eddies. In the central and southern SCS, warm-core anticyclonic eddies start to emerge in March and become full-grown in May. This result confirms the discovery of a SCS warm pool in spring by *Chu et al* [1997]. Furthermore, the dual anticyclonic eddies in the central SCS detected by *Chu et al* [1998a] in May 1995 can be seen in Plate 1 In fact, except in May 1996, which is a La Niño year, such dual anticyclonic eddies were all present in Mays of the years under study. The alongshore currents at the western boundary of the SCS now have reversed direction to become northward, but the magnitudes are small compared to those in winter. The reversal of the direction of the alongshore currents is consistent with the result of the numerical model obtained by *Shaw and Chao* [1994]. In the spring of 1997 and 1998 the warm-core eddies were most energetic. At the Luzon Strait, there is now no clear indication of water exchange between the SCS and the Pacific Ocean.

3.2.3. Summer (June to August). In this season the SCS circulation is largely anticyclonic. Evolving warm-core eddies can be found all over the SCS. East of Vietnam, except in 1995, a cold-core eddy begins to emerge in August. This cold-core eddy has been confirmed by *Kuo and Ho* [1998] using AVHRR temperature images. The northbound alongshore currents east of Vietnam are very energetic in June and July but are weak in August. The alongshore currents turn eastward when reaching the northern boundary of the SCS. At the Luzon Strait the direction of flow now becomes eastward, suggesting that the SCS water enters the Pacific Ocean in summer.

3.2.4. Autumn (September to November). This season marks the change of the circulation system of the SCS from the warm phase to the cold phase. The alongshore currents at the western boundary of the SCS weaken beginning in September and completely reverse direction to become southward in November. In most years the cold-core eddy east of Vietnam formed in August continues to grow and becomes full-grown in November. Also, warm-core eddies are still present in the northern SCS. In general, the Pacific water begins to enter the SCS beginning in November via the Luzon Strait. For no obvious reason the dynamic topography in the autumn of 1996 was unusually high, and the cold-core eddy east of Vietnam virtually disappeared.

3.3. Variations of Circulation at Selected Spots

To supplement the results in Plate 1, we now select two important satellite crossovers, one to the west of the Luzon Strait

Table 1. Comparison of the Kinematic Properties of Drifter-Implied and T/P-Derived Cold-Core Eddies West of Luzon Found in January 1994

	Vorticity	Shearing Deformation	Stretching Deformation	Divergence
T/P cycle 48	3.028 ± 0.195	0.301 ± 0.195	0.808 ± 0.195	0.062 ± 0.195
Drifter 20616	2.770 ± 0.383	0.366 ± 0.383	1.373 ± 0.383	-0.269 ± 0.383

Unit scale in 1×10^{-6} rad s^{-1}

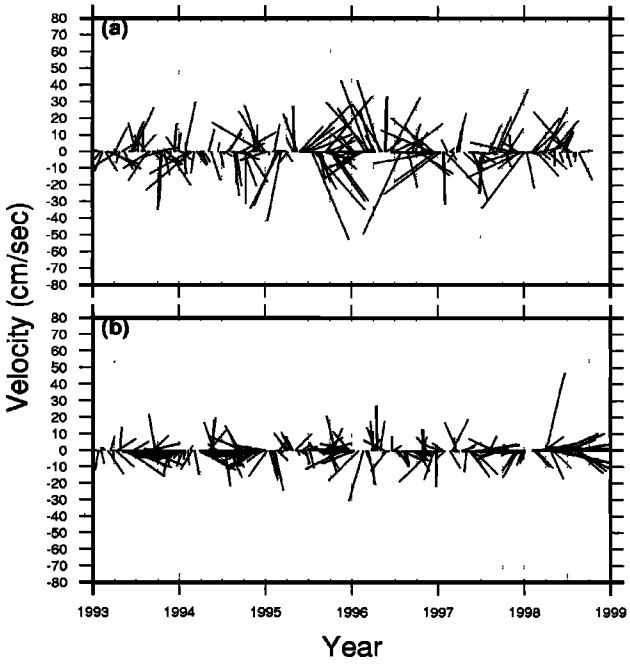

Figure 8. Stick diagrams of currents (a) at crossover A and (b) at crossover B. The locations of A and B are shown in Figure 1.

(crossover A) and the other to the east of Vietnam (crossover B), to see the seasonal and interannual patterns of circulation. The locations of A and B are shown in Figure 1. Figure 8 shows the stick diagrams of the T/P-derived currents at A and B computed with the crossover method. In the actual computations the along-track dynamic heights have been filtered by the Gaussian filter with a 100 km wavelength. We have experimented with many filter wavelengths, but the seasonal patterns can be seen only when the wavelengths of filter are > 100 km. Because our T/P data editing removes bad SSH observations, gaps exist in the two stick diagrams of Figure 8. From Figure 8a the direction of the current west of the Luzon Strait varies over the course of a year, but in general, the direction is mostly northeastward or eastward in spring and summer and is mostly southwestward or westward in winter. The change of the current direction is partly due to water exchange between the SCS and the Pacific Ocean around the Luzon Strait and partly due to the monsoonal wind stress [*Metzger and Hurlburt,* 1996]. In particular, from the spring of 1995 to the spring of 1996 the current west of the Luzon Strait has relatively large velocities. The T/P-derived current at B is rather noisy, probably because this location is near the continental shelf, where T/P has relatively poor data quality. However, from Figure 8b one still can see that the current at B is mostly southwestward or westward in winter and is northeastward or eastward in summer. The change of the current direction at B should be partly due to the monsoonal wind stress and partly due to the bottom topography (see section 4.2 for a detailed discussion). The result here demonstrates that T/P is an important tool for deriving pointwise circulation, and the crossover method can be used to monitor currents in other regions.

3.4. Kinematics and Variation of Eddies

In Plate 1, we saw the spatial and temporal variability of cold- and warm-core eddies; now we will compute the locations of the eddy centers and their kinematic properties. The eddies in Plate 1 are based on monthly averages, so eddies with lifetimes shorter than a month are not identified. In order to have a higher temporal resolution we use the original 10 day dynamic height grids to locate eddies. Because of data gaps and the use of the median filter, we will just compute the kinematic properties for eddies with radii larger than 150 km. As discussed in section 2.2.3, our edge detection of eddy is based on visual inspection of the 210 contour plots and the 210 circulation plots, and the kinematic properties are computed using the least squares method described in Appendix A. Figure 9 shows the distribution of eddies found using our method. In most cases a 10 day snapshot of the dynamic height from T/P contains more than one eddy. Although eddies may be found almost anywhere in the SCS (off the shelf), relatively high densities are found to the east of Vietnam, west of Luzon, and east of the Paracel Islands. The eddies east of the Paracel Islands and east of Vietnam are mostly warm-cored, while the eddies in the northern SCS are mostly cold-cored. The numbers of warm- and cold-core eddies west of Luzon are almost identical. Furthermore, the distribution of eddies is found to be sparse near the boundary of the SCS basin and near the shallow waters of the southern SCS. An eddy can easily change its shape, size, angular velocity, and other properties during the course of evolution, so many of the eddies in Figure 9 actually originated from the same sources.

Table 2 shows the statistics of the kinematic properties of the eddies in Figure 9. From Table 2 the averaged vorticities of the cold-core and warm-core eddies are quite close Both types of eddies have small divergences that are about one one thousandth of their vorticities. The shearing and stretching deformations of cold-core eddies are much larger than those of warm-core eddies, indicating that in general, the cold-core eddies are more deformed and noncircular. Because of the mathematical models used, the standard errors of the estimated vorticity, shearing and stretching deformations, and divergences are the same, and the averaged standard error is 0.143×10^{-6} rad s^{-1}. Also, the averaged standard error of the estimated locations of the centers of eddies is 30 km. For both types of eddy the angular velocities are mostly $< 1 \times 10^{-6}$ rad s^{-1}, and they have no clear dependence on the radial distances. If we assume that the mean radius of the T/P-derived eddies is 250 km, then with a 1×10^{-6} rad s^{-1} angular velocity the tangential velocity is 25 cms^{-1} at the border of the mean eddy, which is about the average of the tangential surface velocities of 10-40 cm s^{-1} of the eddies discovered by *Chu et al* [1998a]. Figure 10 shows the relationship between the radius and the angular velocity of an eddy. In general, the smaller the radius of an eddy, the larger the angular velocity. Assuming that a time-varying eddy has a constant mass, this radius-angular velocity relationship seems to conform to the law of energy conservation. Remarkably, the slopes of the radius-angular velocity relationship for the cold-core and warm-core eddies are almost the same and are $\sim -4 \times 10^{-9}$ rad s^{-1} km^{-1}

Figure 11 shows the monthly numbers of eddies for 1993-1999. In the winter of 1995-1996, which was during a La Niña event, the number of cold-core eddies was relatively large Normally, warm-core eddies existed only from spring to summer, but they existed throughout most of 1997. In the summers of 1995 and 1998 the numbers of warm-core eddies were relatively large. Perhaps the most interesting phenomenon about eddies is the presence of both

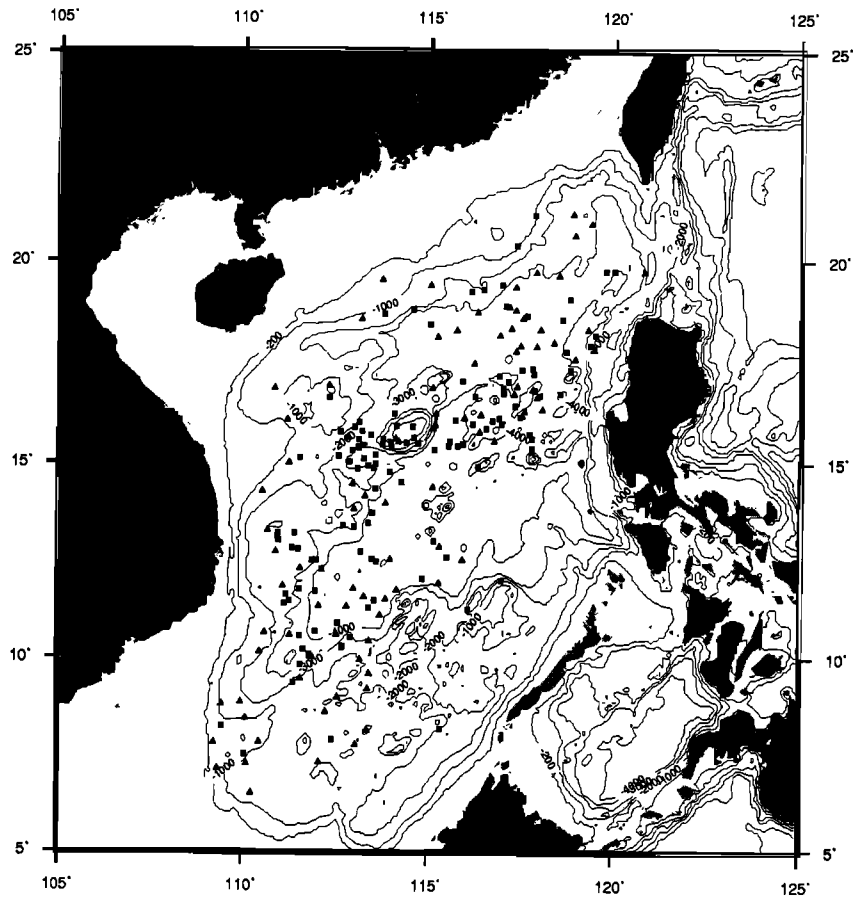

Figure 9. Distribution of cold-core eddies (triangles) and warm-core eddies (squares).

cold-core and warm-core eddies in the waters east of Vietnam, west of Luzon and west of Luzon Strait in different seasons of a year. However, the times of the occurrences of these eddies and the way they evolved varied from year to year. As an example, Table 3 shows by year the occurring times of the first warm-core and cold-core eddies east of Vietnam. The times in Table 3 were obtained by inspecting all the eddies found in Figure 9 but focusing on those near spring and summer. On the basis on Table 3, in 1997 and 1998 the warm-core eddies east of Vietnam occurred earlier in January, and in 1997 the cold-core eddy occurred much earlier than the average, August. If the mechanisms that create these eddies have to do with the monsoonal winds, then the phase

Table 2. Statistics of Kinematic Properties of Eddies Over the South China Sea

	Mean	Standard devivation	Minimum	Maximum
	Cold-Core Eddies (Unit: 1×10^{-6} rad s^{-1}), Number of Eddies = 94			
Vorticity	1.684	1.425	0.343	5.034
Shearing deformation	0 215	0.553	-1.285	3.719
Stretching deformation	0.141	0.233	-1.531	1.197
Divergence	-0.003	0.134	-0.623	0.635
	Warm-Core Eddies (Unit: 1×10^{-6} rad s^{-1}), Number of Eddies = 124			
Vorticity	-1.738	2.256	-4.258	-0.077
Shearing deformation	0.090	0.457	-1.388	1.806
Stretching deformation	-0.078	0.496	-1.251	1.102
Divergence	-0.004	0 010	-0.394	0.294

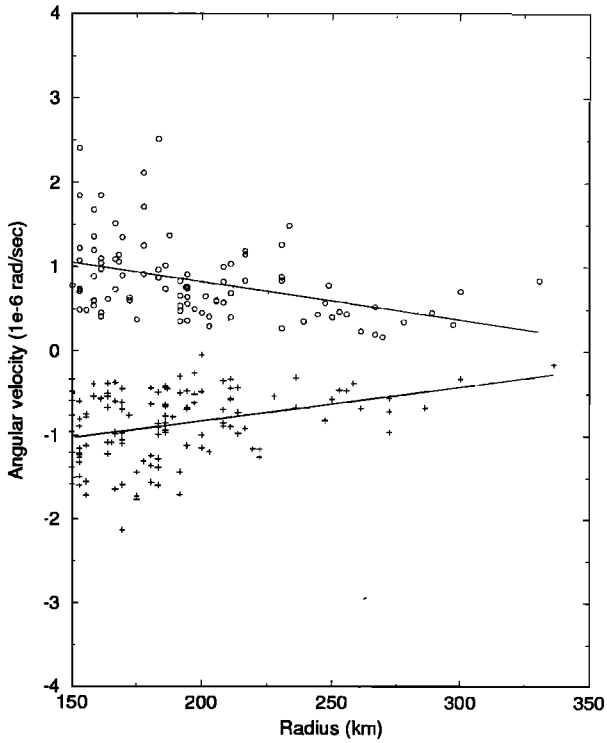

Figure 10. Angular velocities with respect to the radii of eddies. Positive and negative velocities correspond to cyclonic and anticyclonic eddies.

shifts of the eddies in Table 3 can again be linked to ENSO because ENSO has been shown to modulate the monsoonal winds interannually [*Xie et al*, 1998].

4. Discussions

4.1. The Role of Wind on Circulation

Recent studies of the SCS by, for example, *Shaw et al.* [1999], *Wu et al* [1998], and *Chu et al.* [1998b] indicate that wind is the major driving force of the SCS circulation. In discussing the effect of wind on the SCS circulation, there is also a difference between wind stress and wind stress curl [*Shaw et al.*, 1999]. To see the relationship between circulation and wind, we obtained the weekly $1° \times 1°$ gridded wind stress and wind stress curl over the SCS from Centre ERS d'Archivage et de Traitement (CERSAT), France. These wind data are derived from the ERS-1 and ERS-2 scatterometers [see *Maroni*, 1995]. Figure 12 shows the 5 year averaged monthly wind stress curl over the SCS (wind stress is not shown here; seasonal wind stress similar to that derived from ERS-1 and ERS-2 data is given by, for example, *Shaw and Chao* [1994]). On average, the northeasterly winter monsoon begins in September, reaches a peak in December, and then weakens in April The southwesterly summer monsoon begins in May, reaches a peak in August, and then weakens in September [see *Xie et al*, 1998]. Both circulation and wind are strongest in winter and weakest in spring. To compare with the T/P-derived time-varying circulation, we obtained wind stress anomaly (WSA) and wind stress curl anomaly (WCA) by subtracting the respective time-averaged values from the original wind data. To quantify the relationship between circulation and wind, we use the eddy kinetic energy (EKE) per unit mass as the descriptor of circulation [see *Garraffo et al.*, 1992]. EKE is defined as

$$K_e = \frac{1}{2}(u^2 + v^2) \tag{17}$$

Typically, a high EKE is associated with a high variability of circulation [see *Shum et al.*, 1990; *Stammer*, 1997]. We then computed time series of area-averaged EKE, WSA and WCA over the SCS. For comparison, EKE, WSA, and WCA were normalized as [*Hwang and Chen*, 2000]

$$y = \frac{x - \bar{x}}{s_x}, \tag{18}$$

where x and y are the original and normalized values, respectively, and $\bar{x}$ and S_x are the mean and the standard deviation of x, re-

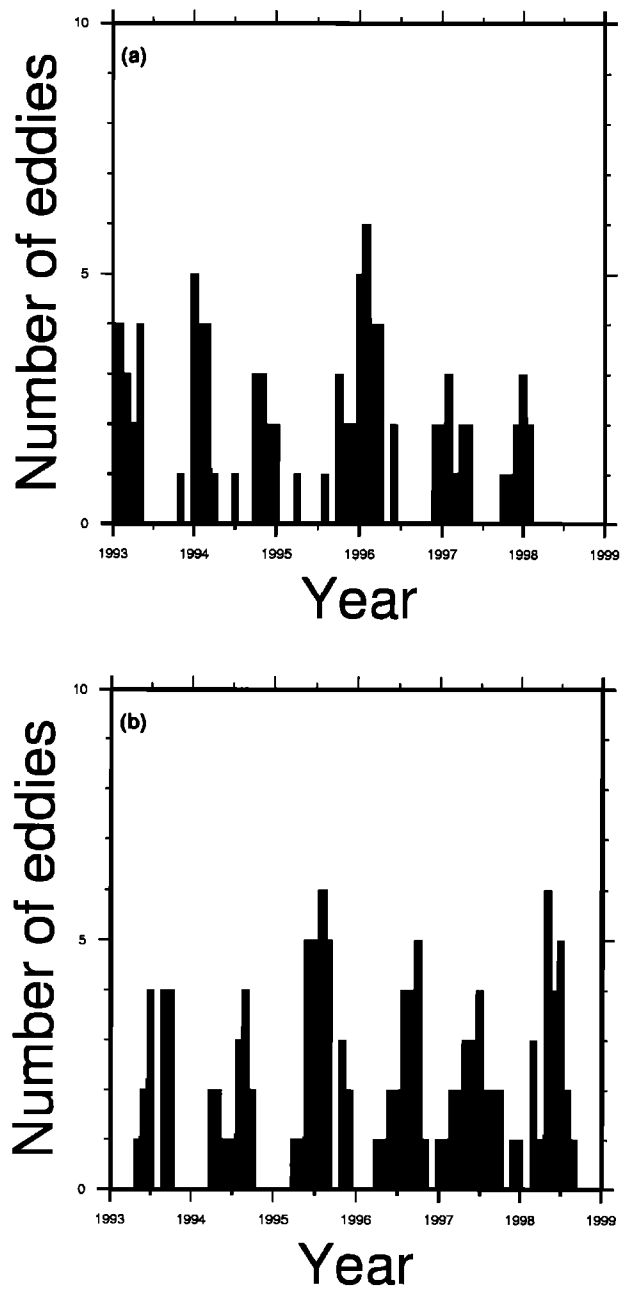

Figure 11. Number of eddies in a month for (a) cold-core eddies and (b) warm-core eddies.

Table 3. Dates of the Occurrences of the First Warm-Core and Cold-Core Eddies East of Vietnam from 1993 to 1998

Year	Warm-Core Eddy	Cold-Core Eddy
1993	March 25	August 21
1994	March 27	August 3
1995	March 19	September 23
1996	April 9	August 16
1997	January 31	July 9
1998	January 13	Not available

spectively. The means of EKE, WSA and WCA are 89 $cm^2 s^{-2}$, 3×10^{-5} Pa, and -3×10^{-12} Pa m^{-1}, respectively, and the standard deviations are 28 $cm^2 s^{-2}$, 0.04 Pa, and 0.33×10^{-7} Pa m^{-1}, respectively. Figures 13a and 13b show the time series of normalized EKE, WSA, and WCA and their power spectra. Both EKE and WSA were strongest in the winter of 1995-1996 and were weakest in the winter of 1997-1998. WCA was strongest in the winter of 1996-1997 weaker in the winter of 1993-1994, and weakest in the winter of 1994-1995. The most peculiar behavior of EKE occurred in the winter of 1997-1998 and in the spring of 1998. First, the peak of EKE in 1997 did not occur in winter as in other years. Second, an unexpected local minimum of EKE occurred in the winter of 1997-1998, and from then on, EKE started to increase. Such a reversal of trend in winter was very unusual because in other years, this reversal occurred in spring. This peculiar behavior of EKE is probably the result of a relatively weak wind field in 1997 and 1998 under the influence of the 1997-1998 El Niño. Furthermore, the largest components of the three time series are the annual components, followed by the semiannual components. In the case of WSA the peak to peak of the winter monsoon from one year to the next forms the annual cycle, while the intervening, relatively weak summer monsoon creates the semiannual cycle .

We first compute the correlation coefficients among EKE, WSA, and WCA in two cases, which are shown in Table 4. In case A we use the raw time series, while in case B we use the time series with the annual components removed. For each pair we also use the Fourier transform to compute the time lag at which the correlation is maximized [*Press et al.*, 1993, p. 538]. The time lags are from zero to 2 months; use of them slightly increases the correlation coefficients but does not change the significances of the correlations in Table 4. In case A the correlation coefficient between EKE and WSA is higher than that between EKE and WCA, and the former is statistically significant according to the testing hypothesis of *Press et al.* [1993, p. 630]. The low correlation between EKE and WCA suggests that the circulation is not due to WCA. WSA and WCA, which are all results of the same monsoonal winds, have a relatively large, significant correlation coefficient of 0.64. Because wind in the SCS is mostly seasonal and is the major driving force of circulation, the seasonal cycle of EKE must be largely due to the seasonal cycle of wind. Thus the high correlation between EKE and WSA is a result of their seasonal cycles, and their correlation will be significantly reduced when their annual components are removed, as in case B.

However, the above correlation analysis does not consider correlations at different frequencies. The alternative is to use coherence analysis, which is similar to correlation analysis but is considered a more powerful tool than the latter [*Bendat and Piersol*, 1993]. The coherence between x and y time series is a function of frequency and is defined as

$$\hat{\gamma}_{xy}^2(f) = \frac{|G_{xy}(f)|^2}{G_{xx}(f)G_{yy}(f)}, \tag{19}$$

where $0 \le \hat{\gamma}_{xy}^2 \le 1$ (from zero correlation to full correlation), f is frequency, G_{xy} is the cross-spectrum between x and y, and G_{xx} and G_{yy} are the autospectra of x and y, respectively. Numerical techniques for estimating $\hat{\gamma}_{xy}^2(f)$ are given by *Bendat and Piersol* [1993]. Data noise will reduce coherence, and its effect is included in the cross spectra and autospectra in (19). The standard error associated with the estimate in (19) is

$$\sigma_\gamma(f) = \frac{\sqrt{2}\left[1-\hat{\gamma}_{xy}^2(f)\right]}{\left|\hat{\gamma}_{xy}^2(f)\right|\sqrt{n}}, \tag{20}$$

where n is the number of data points. According to (20) the larger the coherence, the smaller the standard error. Also, the record length should be as long as possible to reduce the standard error. Given our data record length of 5.6 years, the best choice is to have two overlapped segments in the ensemble averaging, which yields a frequency resolution of 0.375 cycle yr^{-1}. This frequency resolution will allow us to see the coherences at frequencies from bimonthly to interannual. Since there is no rigorous way to determine whether a coherence is statistically significant, we adopt the following empirical rule: if $\hat{\gamma}_{xy}^2(f) \ge 0.5$ and the null hypothesis H_0: $\gamma_{xy}^2(f) = 0$ is rejected, then the correlation between x and y at frequency f is statistically significant. Here we assume $\hat{\gamma}_{xy}^2(f)$ follows the normal distribution with a variance of $\sigma_\gamma^2(f)$. In addition, a 0.5 coherence means the signal-to-noise ratio is one. Figures 13c, 13d, 13e and 13f show the coherences and the phase

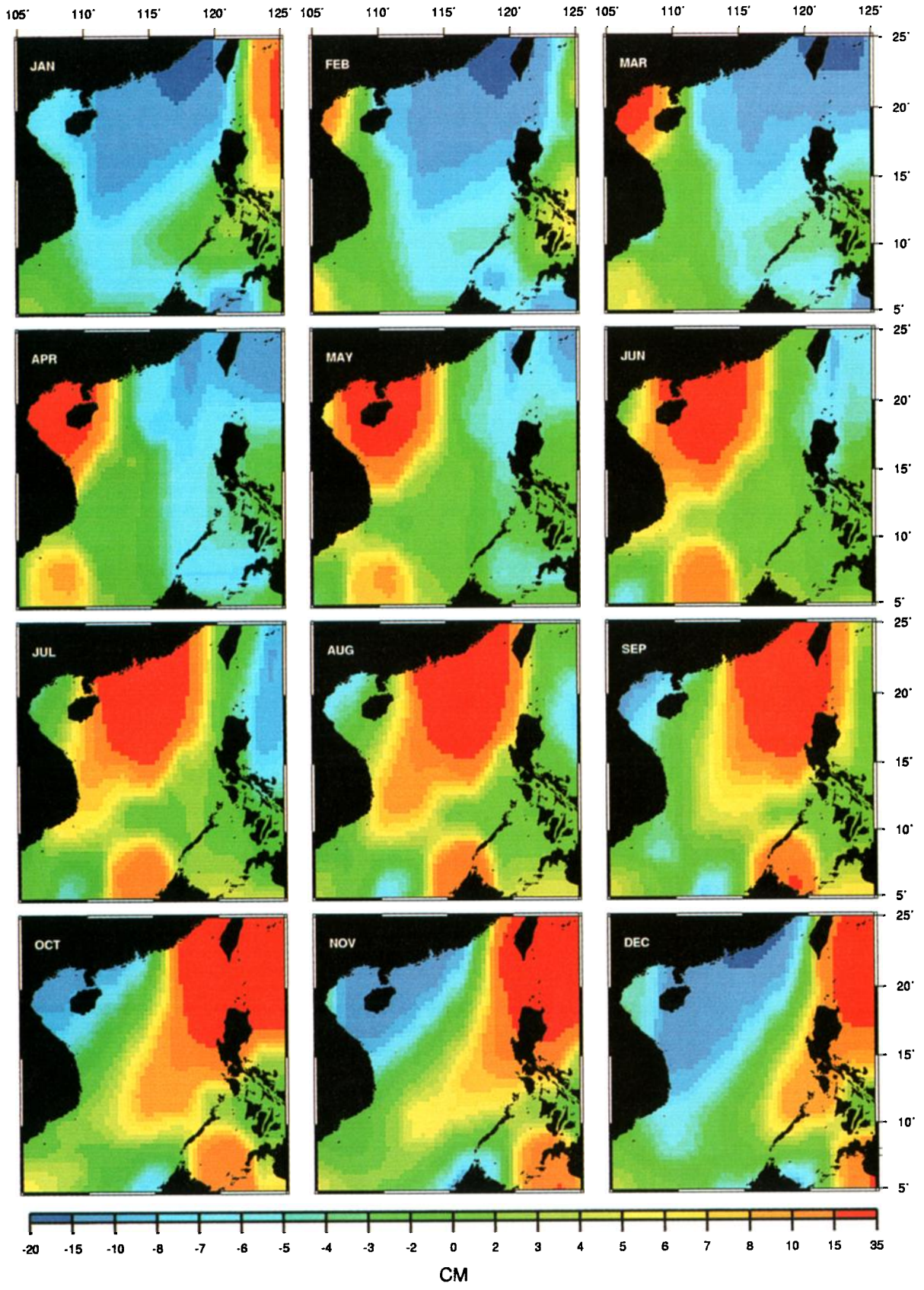

Plate 3. Seven-year averaged monthly steric anomalies of the SCS.

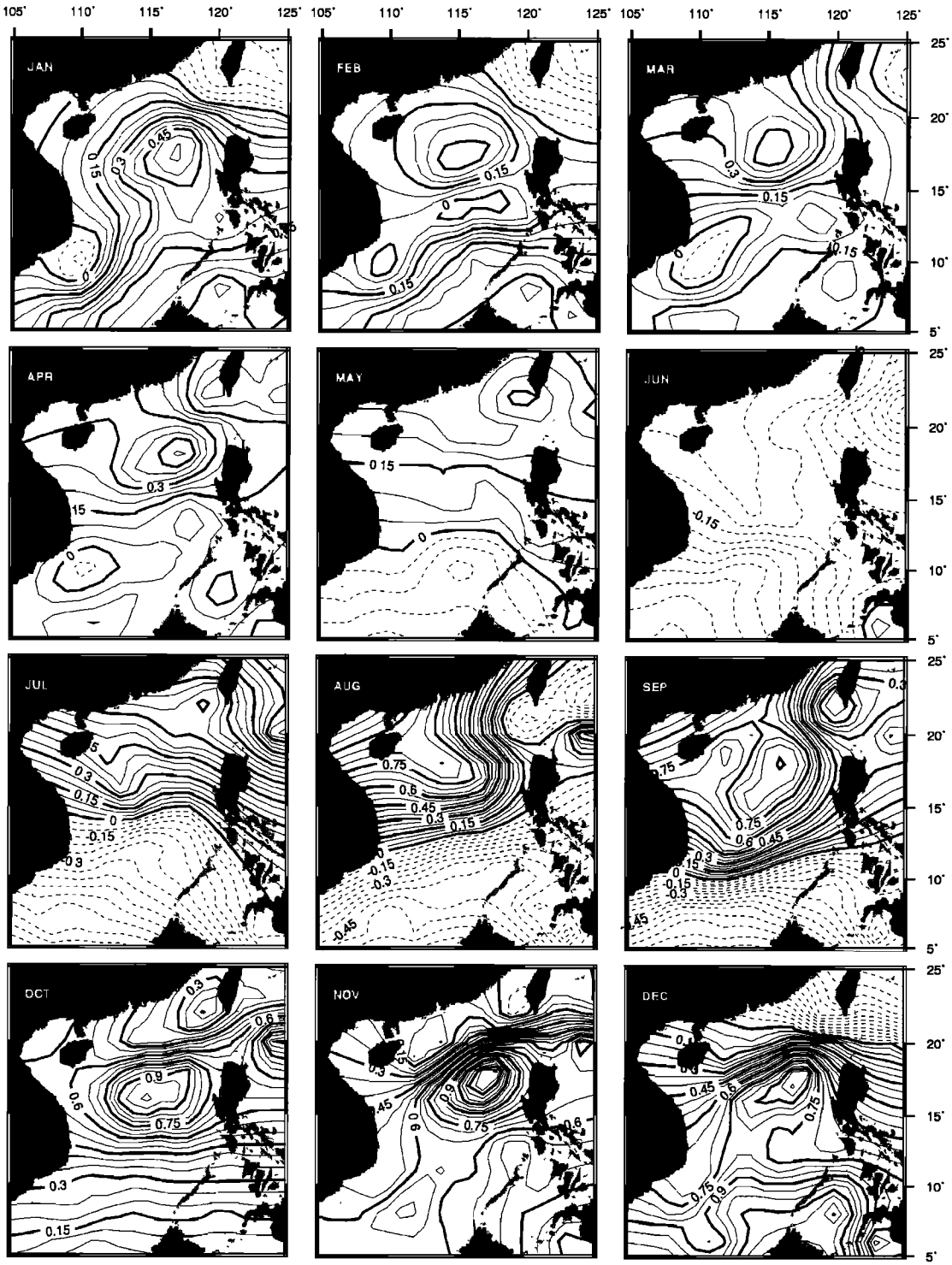

Figure 12. Five-year averaged monthly wind stress curl over the SCS from ERS-1 and ERS-2 scatterometer data. The unit of contours is 10^{-7} Pa m^{-1}.

differences for the WSA-EKE and WCA-EKE relationships. (In a relationship like WSA-EKE or WCA-EKE, WSA or WCA is the input and EKE is the output; in case of a positive phase difference of $\phi(f)$ the input leads the output by $\phi(f)/2\pi f$ in time). In Figs. 13c, 13d, 13e and 13f we also include the 1σ confidence intervals (equivalent to 68% confidence intervals) in the coherence and phase plots. (Because of the short data record that yields large standard errors of $\hat{\gamma}^2_{xy}(f)$, a 99% confidence interval using three sigma's will make some coherence values larger than 1 and is not used). At frequencies of 0.375, 0.750, and 1.125 cycles yr^{-1}, the coherences between WSA and EKE are ~ 0.9 and are statistically significant, suggesting that the interannual and the annual compo-

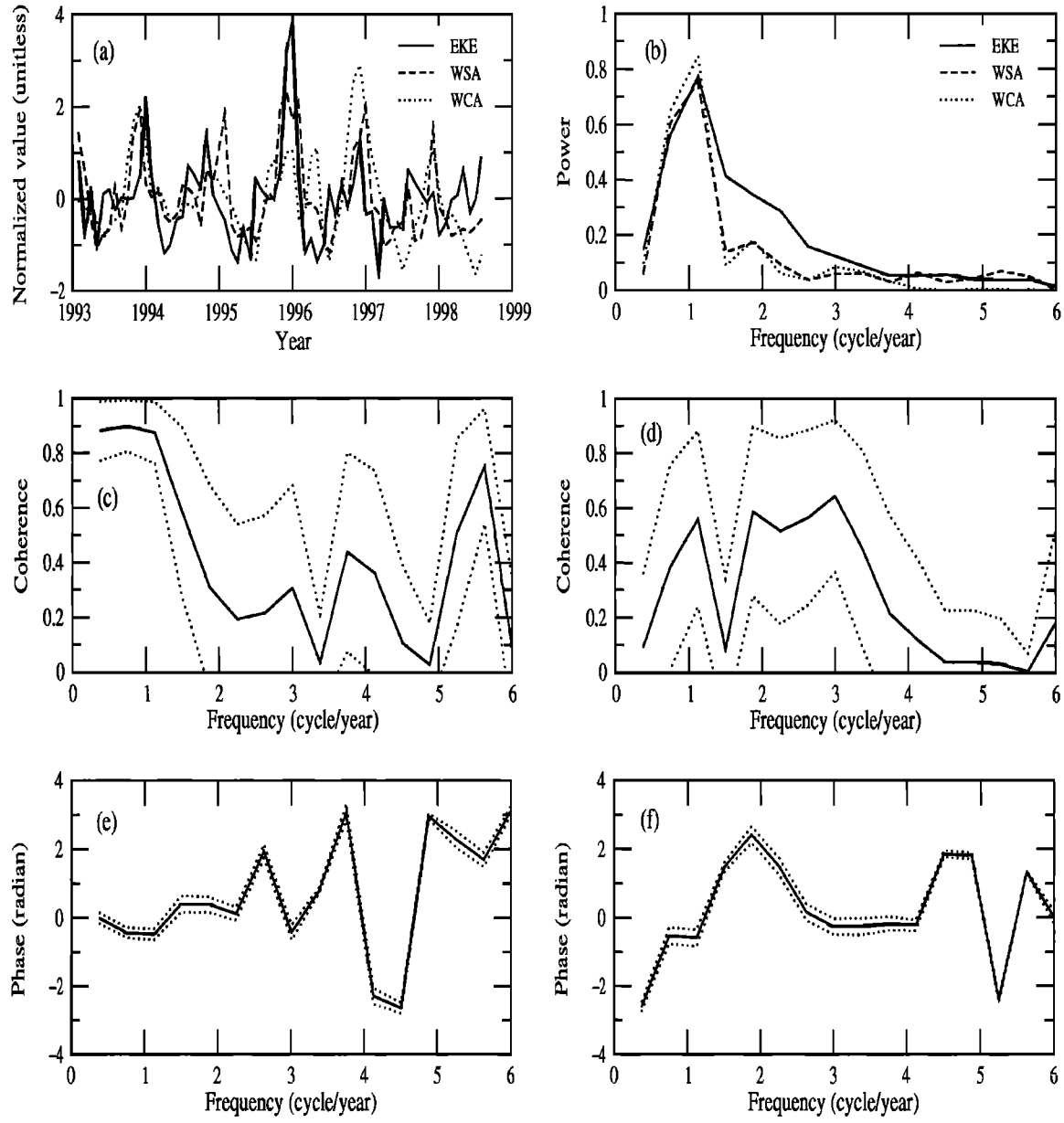

Figure 13. (a) Time series of normalized EKE, WSA, and WCA (b) their power spectra, (c) the coherence between EKE and WSA, (d) the coherence between EKE and WCA, (e) the phase of WSA-EKE, and (f) the phase of WCA-EKE In Figure 13c, 13d, 13e and 13f the dotted lines represent the 68% (1 standard error) confidence intervals.

nents of circulation and wind stress are highly correlated Furthermore, the almost zero phase differences at these frequencies indicate that circulation responds to wind stress immediately. At 5 625 cycles yr^{-1} the coherence between WSA and EKE of 0.75 is significant 0.75, meaning that the 60 day components of circulation and wind stress are highly correlated. However. the coherence between WSA and EKE at the semiannual component is not significant. In contrast to the WSA-EKE relationship, the coherences between WCA and EKE are not significant (near or below 0.5) at the interannual and annual components, but are significant (above 0.6) at the semiannual and the 90 day components. This coherence analysis indicates that both wind stress and wind stress curl contribute to the variation of the SCS circulation, but each has different degrees of contribution at different frequencies.

4.2. Wind Stress and Alongshore Currents East of Vietnam

The alongshore currents east of Vietnam as shown in Plate 1 and Figure 8b have a very distinct seasonal reversal pattern *Chu et al.* [1998b], based on their numerical result of the Princeton Ocean Model (POM), conclude that the alongshore currents east of Vietnam are largely caused by the lateral boundary forcing at the western boundary of the SCS We now investigate how wind stress affects the alongshore currents. To get a representative behavior of the alongshore currents, we use an area-averaged current east of Vietnam, rather than the relatively noisy point current at

Table 4. Correlation Coefficients Among EKE, WSA, and WCA

	EKE	WSA	WCA
	Correlation Coefficients Among Raw Time Series		
EKE	1		
WSA	0.48	1	
WCA	0.27	0.64	1
	Correlation Coefficients Among Time Series with the Annual Components Removed		
EKE	1		
WSA	0.30	1	
WCA	-0.09	0.23	1

crossover B (see Figure 8b). The wind stress is also area-averaged. We choose the area from 110° to 115° E and from 10° to 20° N to compute the area means. Figures 14a and 14b show the stick diagrams of the area-averaged currents and wind stress. Clearly, both the alongshore currents and the wind stress in summer and in winter are in opposite directions. In addition to the seasonal variation, there exists interannual variation in the alongshore currents and wind stress. In Decembers 1993 and 1995 the southwestward alongshore currents were relatively strong compared to the same month of other years. In December 1997, when the 1997-1998 El Niño was at its peak [see, e.g., Hwang and Chen, 2000], both the southwestward alongshore currents and the wind stress were weak. Moreover, in the winters of 1994-1995 and 1997-1998 the alongshore currents stayed in the southwest direction for just a very short time.

To be more specific about the directions of flows, in Figure 14c we show the time series of the azimuths of the alongshore currents and wind stress east of Vietnam. Both the azimuths of the currents and the wind stress fall mostly into two intervals: [0°, 90°] and [180°, 270°], corresponding to the northeast and the southwest directions. The times of the reversals of currents and wind vary from year to year. In autumn the wind turns southwestward earlier than the alongshore currents, and this shows that the wind leads the currents. In the springs of 1993, 1994, and 1997, again, the wind leads the alongshore currents and turns northeastward earlier than the currents, but surprisingly, in the springs of 1995, 1996, and 1998 the alongshore currents turn northeastward earlier than the wind. This earlier turning of currents in spring toward the northeast can be explained as follows. In the Marches of 1995, 1996, and 1998, for some reason the wind at the western boundary of the SCS is almost westward. By the Ekman effect, the alongshore currents will turn northward. However, the continental shelf of the SCS acts like a wall to divert the alongshore currents toward the northeast. Thus this phenomenon is created by the combined effect of wind stress and the bottom topography at the western boundary of the SCS.

4.3. Wind and Formation of Eddy

Comparing Plate 2 and Figure 12, one gets the impression that there is a high degree of geographic correlation between wind stress curl and an enhanced probability of eddy occurrence, especially in the northern and the central SCS. Conceptually, cyclonic wind stress curl will produce divergence in the surface water and upwelling, anticyclonic wind stress curl will produce convergence and downwelling. Upwelling brings cold water from the deep to the surface and hence creates cold-core eddies; downwelling deepens the thermocline and hence creates warm-core eddies. *Chu et al* [1998b] have used this concept to theorize the formations of cold-core and warm-core eddies in the central SCS basin and then verified their theory using the result from the POM model. Now we will compare wind stress curl and eddies in the central SCS basin. Figure 15 shows the time series of normalized angular velocity and WCA averaged over the area 13°-17° N and 110°-117° E (this area roughly covers the central SCS basin). According to the concept of divergence and convergence we just mentioned the signs of the two time series will follow the same patterns, although phase shifts may exist. Furthermore, positive (negative) WCA should correspond to a cold-core (warm-core) eddy whose angular velocity is positive (negative). Indeed, Figure 15 shows that the overall trends of the two time series agree reasonably well (with phase shifts), but significant discrepancies exist in the springs of 1993 ad 1995 and in the autumn of 1996. Such discrepancies may be caused by anomalies in the T/P altimeter data and the ERS-1 and -2 wind data (for example, typhoons visit the SCS very often and can easily cause anomalies), or the discrepancies may just reveal the possibility that in addition to wind stress curl, there are other factors affecting the formations of eddies in the central SCS basin.

The cold-core eddies east of Vietnam in August (see Plate 1) are again due to upwelling, but the process is different from that in the central SCS basin. That is, in August the southwesterly monsoonal wind stress parallel to the coast of east Vietnam will drive the water to the right of the wind because of the Ekman effect, resulting in upwelling of cold water from below, thereby creating the cold-core eddies. Here wind stress curl plays no role.

4.4. The Effect of Steric Anomaly on Circulation and Eddy

There is a concern as to whether the T/P-derived seasonal variation of circulation and eddy over the SCS is largely a result of the seasonal variation of the steric anomaly due to thermal expan-

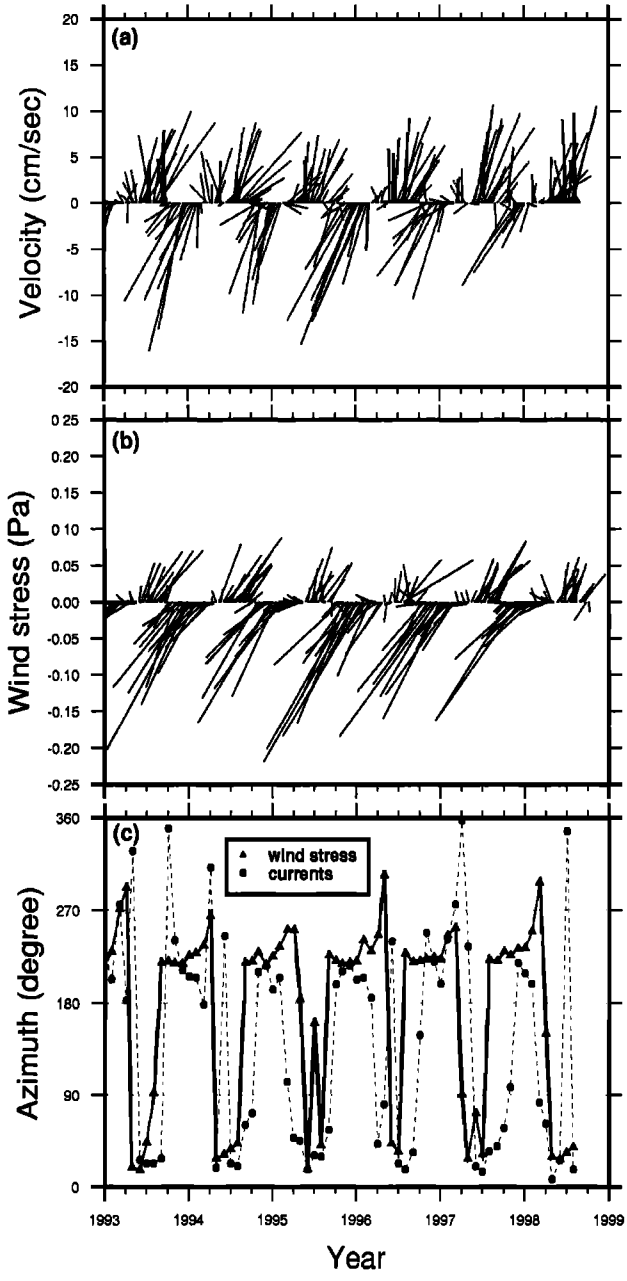

Figure 14. Stick diagrams of (a) the area-averaged alongshore currents and (b) the area-averaged wind stress east of Vietnam at a 10 day interval (c) The azimuths of the currents and wind stress.

sion of seawater. In the open ocean the steric anomaly has a very large spatial scale and its horizontal derivatives are small, thus the steric anomaly contributes little to the time-dependent circulation ((1) and (2) require the horizontal derivatives) [see, e.g., *Chen et al.*, 2000] This is why researchers like *Wunsch and Stammer* [1998] do not remove steric anomalies when computing the time-dependent geostrophic circulations in the open ocean. In the SCS the monsoonal winds blow and the ocean is heated and cooled, resulting in forced seasonal cycles in sea level and circulation. The steric anomaly is part of the results of the interactions among the ocean, wind forcing, and heating and should not be thought of as separate from the forced seasonal cycles. In fact, the response of the SCS to wind and heating is very complicated and may be simulated by suitable dynamic models such as those used by *Shaw and Chao* [1994] and *Metzger and Hurlburt* [1996], who also include temperatures in their models. The response can also be observed by remote sensing tools such as the T/P altimeter, as shown in this study. In addition, if we are interested in the mean flow of the SCS, the steric anomaly can be safely disregarded because it is mostly seasonal and can be averaged out using many years of data.

To see any possible connection between the steric anomaly and the circulation, we computed monthly steric anomalies over the SCS from 1992 to 1999 using a method based on *Polito and Cornillon* [1997] and *Chen et al.* [2000]. Transforming the integral of *Polito and Cornillon* [1997, p.3221] to an approximation that sums over 14 ocean layers [*Chen et al.*, 2000], we have

$$\Delta H_{\text{steric}} = \int_{-Z_{\max}}^{0} \alpha(T,P)\Delta T dz \approx \sum_{i=1}^{14} \alpha_i \Delta T_i H_i \qquad (21)$$

where α_i is the coefficient of thermal expansion from *Gill* [1982, Table A3.1], and ΔT_i is the temperature anomaly relative to the mean of layer ; and H_i is the thickness of layer i [*Chen et al.*, 2000]. The temperature data at different depths of the SCS were taken from the National Oceanographic Data Center (NODC) via the Internet. As the temperature data qualities in different years are not quite consistent, we computed the 7 year averaged monthly steric anomalies, which are shown in Plate 3. Note that the March and September steric anomalies in Plate 3 agree well with those given by *Chen et al* [2000]. The monthly steric anomalies are seasonal and have an average amplitude of ~ 10 cm, with a larger amplitude in the northern SCS. Their spatial patterns and scales

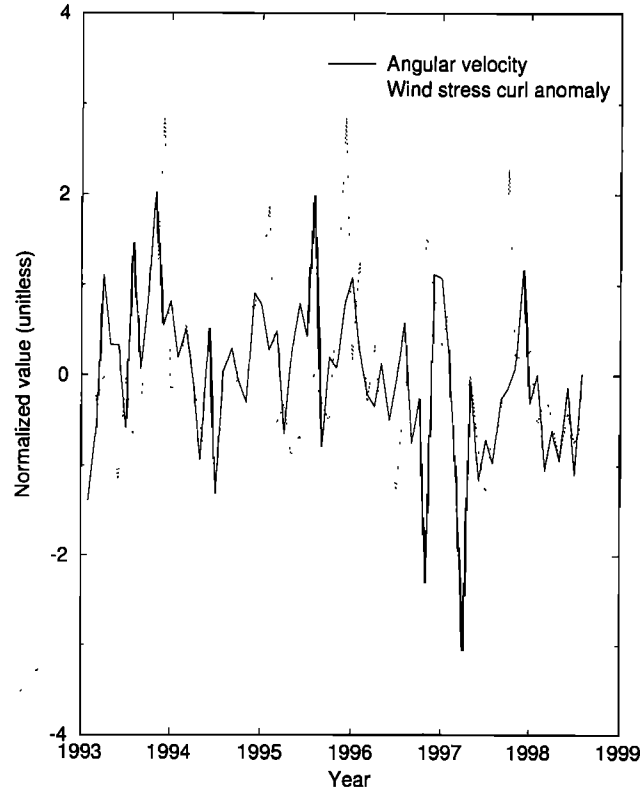

Figure 15. Time series of normalized angular velocity and wind stress curl anomaly over the central SCS basin.

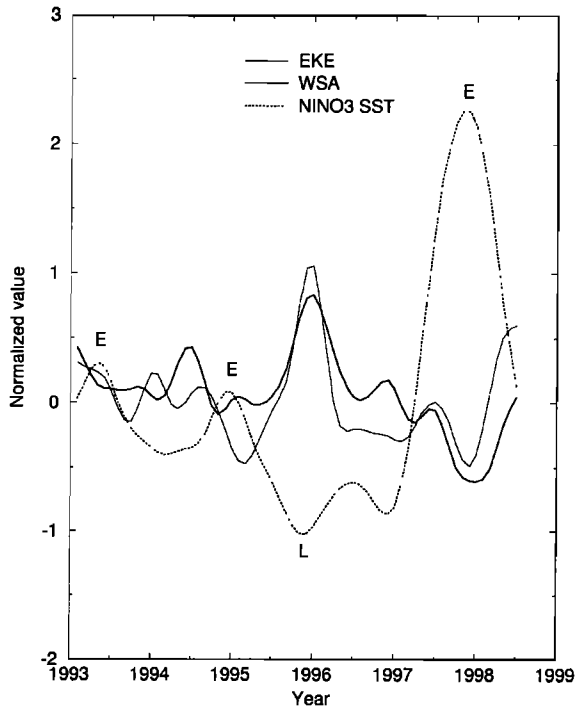

Figure 16. Normalized time series of NINO3 SST and EKE with annual components removed. The letters "E" indicate the peak of an El Niño, and the letter "L" indicates the peak of a La Niña.

are quite different from those of circulations and eddies in Plate 2. For example, from January to March the steric anomalies have local lows extending all over the northern SCS, and their spatial structures are too smooth to be similar to the structures of eddies seen in Plate 2. West of the Hainan Island, a large, nearly circular local high of steric anomaly emerges in March, then drifts to the east, and finally, disappears in December. While drifting, this local high is accompanied by a long, northeast-southwest oriented "tail" to the south. Such a pattern of local high and tail is not seen in Plate 2. Furthermore, on the basis of a comparison between the steric anomaly and dynamic topography patterns the steric anomaly alone should not be responsible for the seasonal reversal of the alongshore currents east of Vietnam. In summary, the T/P-derived circulations and eddies are not solely due to the steric anomaly; they are a result of the complicated response of the SCS to local and perhaps nonlocal wind forcing and heating, as most dynamic models have revealed.

4.5. ENSO and the Interannual Variation of Circulation

In the previous analyses, especially in section 3, we point out that the interannual variation of the SCS circulation may be associated with El Niño/La Niña events. We now wish to quantify their relationship using the EKE and NINO3 SST time series. (Analyses of NINO3 SST in connection with El Niño/La Niña have been made by, for example, *Torrence and Webster* [1998]). First, we did a coherence analysis for the two time series. The result shows that the coherence at 0.375 cycle yr^{-1}, i.e., the interannual component, is only 0.08, which is too small to confirm the correlation between ENSO and the SCS circulation at the interannual timescale This low coherence may have been due to the combined effect of data noise and short record length in both time series. To mitigate this situation, we removed the annual components of both EKE and NINO3 SST and then smoothed the residual time series by the Gaussian filter with a 1 year wavelength. The residual smoothed EKE and NINO3 SST time series, as shown in Figure 16, now have a correlation coefficient of -0.42, which is statistically significant. The peaks of El Niño and La Niña events, based on *Kiladis and Diaz* [1989], are also marked in Figure 16. In Figure 16, the interannual highs (El Niños) and lows (La Niña) of NINO3 SST correspond well to the interannual lows and highs of EKE, with the NINO3 SST peaks leading the EKE peaks by 1-3 months. In 1992-1993 the relationship between the high of NINO3 SST and the low of EKE is not clear because of the edge effect in the Gaussian filtering. During the 1995-1996 La Niña the SCS circulation was exceptionally energetic, resulting in a very prominent EKE high in the winter of 1995-1996. During the three El Niños from 1993 to 1999 the circulations of the SCS were relatively weak, and this weakness agrees with the EOF result of *Wu et al.* [1998]. In Figure 16, we also include the residual smoothed WSA time series, which has a negative significant correlation of -0.80 with the NINO3 SST time series. (Also, the NINO3 SST peaks slightly lead the WSA peaks.) This high correlation suggests that the interannual SCS wind component oscillates with ENSO. Again, since most numerical models show that the SCS circulation is largely wind-driven, it can be concluded that at the interannual timescale, ENSO affects the SCS wind, which in turn affects the SCS circulation.

5. Summary and Conclusions

This study demonstrates that the T/P altimeter with a spatial resolution of ~ 300 km and a temporal resolution of 10 days is a good sensor for observing the mesoscale circulations and eddies in a marginal sea like the SCS. The T/P-derived circulation and eddies are in good agreement with drifter data. We propose a method to compute velocity components of geostrophic flow at the crossovers of two satellite ground tracks. This method can be used to monitor local current and eddy activities. We also introduce a method to identify eddies and compute their kinematic properties. The SCS circulation is largely driven by the monsoonal winds with seasonally varying directions and is modulated interannually by ENSO. Both warm-core and cold-core eddies were present nearly everywhere in the SCS but mostly were concentrated along a band across the SCS basin. The monthly numbers of eddies have interannual variations due to ENSO. The reversal of the alongshore currents east of Vietnam was in complete accordance with wind stress. The angular velocities of cold-core and warm-core eddies over the central SCS basin are coherent with wind stress curl. Finally, the spatial pattern and the scale of the steric anomaly are quite different from those of circulation and eddy. As more T/P-class altimeters such as JASON-1 and ENVISAT are to be deployed in the near future, altimetric monitoring of circulation and eddies over the SCS and any other semi-closed seas can be continued, and the spatial and temporal resolutions will be significantly improved.

Appendix A: Estimating the Kinematic Properties of an Eddy by Least Squares

In the model of (13) and (14) (see section 2.2.3.), let $\beta = [g_{11}, g_{12}, g_{21}, g_{22}, x_0, y_0]^T$ be the vector containing the unknown parameters and let

$$\beta = \beta_0 + \Delta\beta \ , \tag{A1}$$

where β_0 is the approximate vector of β and $\Delta\beta$ is the correction to β_0. Linearizing the observation equations in (13) and (14) and using matrix notations, we have

$$\mathbf{V} = \mathbf{A}\ \Delta\beta\ - \mathbf{L} \tag{A2}$$

where $\mathbf{V}$ is the residual vector containing e_u and e_v, $\mathbf{A}$ is the design matrix, and $\mathbf{L}$ is a vector containing the differences between the T/P-observed velocities and the computed velocities based on β_0. Specifically,

$$\mathbf{V} = \begin{bmatrix} e_{u_1} \\ e_{v_1} \\ \vdots \\ e_{u_n} \\ e_{v_n} \end{bmatrix} , \tag{A3}$$

$$\mathbf{A} = \begin{bmatrix} x_1 - x_0^0 & y_1 - y_0^0 & 0 & 0 & -g_{11}^0 & -g_{12}^0 \\ 0 & 0 & x_1 - x_0^0 & y_1 - y_0^0 & -g_{21}^0 & -g_{22}^0 \\ & & \vdots & \vdots & & \\ x_n - x_0^0 & y_n - y_0^0 & 0 & 0 & -g_{11}^0 & -g_{12}^0 \\ 0 & 0 & x_n - x_0^0 & y_n - y_0^0 & -g_{21}^0 & -g_{22}^0 \end{bmatrix} , \tag{A4}$$

$$\mathbf{L} = \begin{bmatrix} u_1 - u_1^0 \\ v_1 - v_1^0 \\ \vdots \\ u_n - u_n^0 \\ v_n - v_n^0 \end{bmatrix} , \tag{A5}$$

where n is the number of data points (each data point has two velocity components); $g_{11}^0, g_{12}^0, g_{21}^0, g_{22}^0, x_0^0$, and y_0^0 are the elements of β_0; and u_i^0 and v_i^0, $i=1,\ldots, n$ are the approximate velocities computed by substituting $g_{11}^0, g_{12}^0, g_{21}^0, g_{22}^0, x_0^0$, and y_0^0 into (13) and (14). The least squares solution of $\Delta\beta$ can be obtained by minimizing the sum of all squared e_u and e_v, that is [*Koch*, 1987],

$$\Delta\beta = (\mathbf{A}^T\mathbf{A})^{-1}\mathbf{A}^T\mathbf{L} \tag{A6}$$

where we have assumed that all observations have the same weight. Since (A2) is correct to only the first-order term, the estimation must be iterated until all elements in $\Delta\beta$ approach zero. When the estimation of β is completed, its covariance matrix can be computed as

$$\Sigma_\beta = \hat{\sigma}_0^2 (\mathbf{A}^T\mathbf{A})^{-1} \ , \tag{A7}$$

where $\hat{\sigma}_0^2$ is the a posterior variance of unit weight computed as

$$\hat{\sigma}_0^2 = \frac{\mathbf{V}^T\mathbf{V}}{2n-6} \ . \tag{A8}$$

The approximate vector β_0 is estimated as follows. For an eddy with an estimated center and radius the first and second derivatives of the dynamic height within the radius are computed from a quadratic polynomial that best fits the dynamic height (see section 2.2.1). The "observed" velocities are computed from the first derivatives using (1) and (2). The approximate velocity gradients are computed from the second derivatives using

$$g_{11}^0 = -\frac{g}{f}\frac{\partial^2\zeta}{\partial x \partial y} \ , \quad g_{12}^0 = -\frac{g}{f}\frac{\partial^2\zeta}{\partial y^2} \ ,$$

$$g_{21}^0 = \frac{g}{f}\frac{\partial^2\zeta}{\partial x^2} \ , \quad g_{22}^0 = \frac{g}{f}\frac{\partial^2\zeta}{\partial x \partial y} \ . \tag{A9}$$

Thus, in theory we have $g_{11}^0 = -g_{22}^0$, and the approximate divergence is zero. The averaged gradients as computed from (A9) are then used to form the β_0 needed in the first iteration. Typically, after three iterations our method can achieve $\Delta\beta_i / \beta_i \approx 10^{-7}$ (the limit of the single-precision arithmetic), where $\Delta\beta_i$ and β_i are the elements of $\Delta\beta$ and β, respectively.

Acknowledgments. This research was supported by the National Science Council of Taiwan under contract NSC88-2611-M-009-001-AP7. The suggestions from P. Cornillon and three anonymous reviewers greatly improved the quality of this paper. The comments of C. Wunsch, C. K. Shum, and J. L. Chen on the steric anomaly effect were very useful. This is a contribution to the SCSMEX project.

References

Apel, J. R., *Principles of Ocean Physics*, 634 pp., Academic, San Diego, Calif., 1987.

Archivings, Validation and Interpretation of Satellite Oceanographic data (AVISO), *AVISO User Handbook for Merged TOPEX/Poseidon Products*, 3rd ed., 1996.

Bendat, J. S., and A. G. Piersol, *Engineering Applications of Correlation and Spectral Analysis*, 2nd ed., 458 pp., John Wiley, New York, 1993.

Chen, J. L., C. K. Shum, C. R. Wilson, D. P. Chambers, and B. D. Tapley, Seasonal sea level change from TOPEX/Poseidon observation and thermal expansion, *J. Geod.*, *73*, 638-647, 2000.

Chu, P. C., S. Liu, and Y. Chen, Temporal and spatial variabilities of the South China Sea surface temperature anomaly, *J. Geophys. Res.*, 102, 20,937-20,955, 1997.

Chu, P. C., C. W. Fan, C. J. Lozano, and J. Kirling, An airborne expendable bathythermograph survey of the South China Sea, May 1995, *J. Geophys. Res.*, *103*, 21,637-21,652, 1998a.

Chu, P. C., Y. Chen, and S. Lu, Wind-driven South China Sea basin warm-core/cool-core eddies, *J. Oceanogr.*, *54*, 347-360, 1998b.

Crawford, W. R., and F. A. Whitney, Mesoscale eddy aswirl with data in Gulf of Alaska, *Eos Trans. AGU*, *80*, 365, 1999.

Dale, W. L., Winds and drifter currents in the South China Sea, *Malay. J. Trop. Geogr.*, *8*, 1-31, 1956.

Eanes, R., and S. Bettadpur, The CSR 3.0 global ocean tide model, *Res. CSR-TM-95-06*, Cent. for Space Res., Univ. of Tex., Austin, 1995.

Fu, L.-L., E. J. Christensen, C. A. Yamarone Jr., M. Lefebvre, Y. Menard, M. Dorrer, and P. Escudier, TOPEX/Poseidon mission overview, *J. Geophys. Res.*, 99, 24,369-24,382, 1994.

Garraffo, Z., S. L. Garzoli, W. Haxby, and D. Olson, Analysis of a general circulation model, 2, Distribution of kinetic energy in the South Atlantic and Kuroshio/Oyashio systems, *J. Geophys. Res.*, 97, 20,139-20,153, 1992.

Gerald, C. F., and P. O. Wheatley, *Applied Numerical Analysis*, 5th ed., 748 pp., Addison-Wesley, New York, 1994.

Gill, A. E., *Atmosphere-Ocean Dynamics*, 662 pp., Academic, San Diego, Calif., 1982.

Grundlingh, M. L., Tracking eddies in the southeast Atlantic and south-

west Indian Oceans with TOPEX/Poseidon, *J Geophys Res*, *100*, 24,977-24,986, 1995

Hansen, D V, and P -M Poulain, Quality control and interpolation of WOCE/TOGA drifter data, J *Atmos Oceanic Technolo*, *13*, 900-909, 1996

Heiskanen, W A, and H Moritz, *Physical Geodesy*, 364 pp, Inst of Phys Geodesy, Tech Univ Graz, Graz, Austria, 1985

Hu, J -H, Study on surface currents in the South China Sea, paper presented at Workshop of Oceanography, Hsinchu, Taiwan, NSC, 1998

Hwang, C, A study of Kuroshio's seasonal variabilities using a gravimetric-altimetric geoid and TOPEX/Poseidon altimeter data, *J Geophys Res*, *101*, 6313-6335, 1996

Hwang, C, Analysis of some systematic errors affecting altimeter-derived sea surface gradient with application to geoid determination over Taiwan, *J Geod*, *71*, 113-130, 1997

Hwang, C, and S -A Chen, Fourier and wavelet analyses of TOPEX/Poseidon-derived sea level anomaly over the South China Sea a contribution to SCSMEX, *J Geophys. Res*, in press, 2000

Hwang, C, E -C. Kao, and B Parsons, Global derivation of marine gravity anomalies from Seasat, Geosat, ERS-1 and TOPEX/Poseidon altimeter data, *Geophys J. Int*, *134*, 449-459, 1998

Kiladis, G N, and H. F. Diaz, Global climatic anomalies associated with extremes in the Southern Oscillation, *J Clim*, *2*, 1069-1090, 1989

Kirwan, A D, Jr, W J Merrell Jr, J K Lewis, R E Whitaker, and R Legeckis, A model for the analysis of drifter data with an application to a warm core ring in the Gulf of Mexico, *J Geophys Res*, *89*, 3425-3438, 1984

Koch, K. R, *Parameter Estimation and Hypothesis Testing in Linear Models*, 378 pp., Springer-Verlag, New York, 1987

Kuo, N -J, and C.-R Ho, Satellite observations of surface temperature of the South China Sea, paper presented at Workshop of Oceanography, Hsinchu, Taiwan, NSC, 1998

Lau, W K -M., South China Sea monsoon experiment observed from satellites, *Eos Trans AGU*, *78*, 599, 603, 1997

Lemoine, F G, et al, The development of the Joint NASA GSFC and the National Imagery and Mapping Agency (NIMA) geopotential model EGM96, *NASA Tech Pap. TP-1998-206861*, 575 pp, 1998

Maroni, C, The quarterly topic Offline wind field production, *CERSAT News*, *5*, 2-3, 1995

Metzger, E J., and H E. Hurlburt, Coupled dynamics of the South China Sea, the Sulu Sea and the Pacific Ocean, *J Geophys Res*, *101*, 12,331-12,352, 1996

Meyers, S. D, and S. Basu, Eddies in the eastern Gulf of Alaska from TOPEX/Poseidon altimetry, *J Geophys. Res*, *104*, 13,333-13,344, 1999

Naess, O E, and L Bruland, Improvement of the multichannel, seismic data through the applications of the median concept, *Geophys Prospesct*, 37, 225-241, 1989

Nitani, H, Beginning of the Kuroshio, in *Kuroshio Its Physical Aspects*, edited by H Stommel and K Yoshida, pp 129-163, Univ of Tokyo Press, Tokyo, 1972

Okubo, A, Horizontal dispersion of floatable particles in the vicinity of velocity singularities such as convergences, *Deep Sea Res*, *Oceangr Abstr*, *17*, 445-454, 1970

Polito, P S, and P Cornillon, Long baroclinic Rossby waves detected by TOPEX/Poseidon, *J Geophys. Res*, *102*, 3215-3235, 1997

Press, W H, S A Teukolsky, B. P. Flannery, and W T Vetterling, Numerical Recipes. 2nd ed, Cambridge Univ. Press, New York, 1993.

Sanderson, B G, Structure of an eddy measured with drifters, *J Geophys Res*, *100*, 6761-6776, 1995

Schlax, M G, and D B Chelton, Aliased tidal errors in TOPEX/Poseidon sea surface height data, *J Geophys Res*, *99*, 24,761-24,775, 1994

Shaw, P -T, The season variation of the intrusion of the Philippines Sea into the South China Sea, *J Geophys Res*, *96*, 821-827, 1991

Shaw, P -T, and S.-Y Chao, Surface circulation in the South China Sea, *Deep Sea Res*, *Oceangr Abstr*, *41*, 1663-1683, 1994.

Shaw, P -T, S -Y Chao, and L -L Fu, Surface height variations in the South China Sea from satellite altimetry, *Oceanol. Acta*, *22*, 1-17, 1999

Shum, C K, R A Werener, D T Sandwell, B. H. Zhang, R. S Nerem, and B D Tapley, Variations of global mesoscale eddy energy observed from Geosat, *J Geophys Res*, *95*, 17,865-17,876, 1990

Siegel, D. A, D J McGillicuddy Jr, and E A Fields, Mesoscale eddies, satellite altimetry and new production in the Sargasso Sea, *J Geophys Res*, *104*, 13,359-13,380, 1999

Smith, W. H F, and P Wessel, Gridding with continuous curvature splines in tension, *Geophysics*, *55*, 293-305, 1990

Soong, Y S, J H Hu, C R. Ho, and P P Niiler, Cold-core eddy detected in South China Sea, *Eos Trans AGU*, *76*, 345, 347, 1995

Stammer, D., Global characteristics of ocean variability estimated from regional TOPEX/Poseidon altimeter measurements, *J Phys. Oceanogr*, *27*, 1743-1769, 1997

Torrence, C, and P J Webster, The annual cycle of persistence in the El Niño/Southern Oscillation, *Q J. R Meteorol Soc*, *124*, 1985-2004, 1998

Wu, C -R, P.-T Shaw, and S.-Y Chao, Seasonal and interannual variations in the velocity field of the South China Sea, *J Oceangr*, *54*, 361-372, 1998

Wunsch, C, and D Stammer, Satellite altimetry, the marine geoid, and the oceanic general circulation, *Annu. Rev Earth Planet Sci*, *26*, 219-253, 1998

Wyrtki, K, Scientific results of marine investigations of the South China Sea and Gulf of Thailand 1959-1961, *Naga Rep 2*, pp 164-169, Scripps Inst. of Oceanogr, Univ. of Calif, San Diego, 1961

Xie, A., Y -S Chung, X. Liu, and Q Ye, The interannual variations of the summer monsoon onset over the South China Sea, *Theor Appl. Climatol.*, *59*, 201-213, 1998

S -A Chen and C Hwang, Department of Civil Engineering, National Chiao Tung University, 1001 Ta Hsueh Road, Hsinchu, Taiwan. (hwang@geodesy cv nctu.edu tw)

(Received March 30, 1999, revised May 5, 2000,
accepted May 9, 2000)